NASA TECHNICAL MEMORANDUM

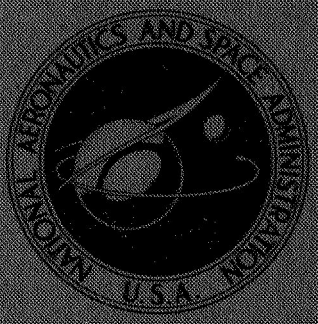

NASA TM X-1842

NASA TM X-1842

EXPERIMENTAL INVESTIGATION OF DYNAMIC DISTORTION IN A MACH 2.50 INLET WITH 60 PERCENT INTERNAL CONTRACTION AND ITS EFFECT ON TURBOJET STALL MARGIN

by James E. Calogeras

Lewis Research Center
Cleveland, Ohio

NATIONAL AERONAUTICS AND SPACE ADMINISTRATION • WASHINGTON, D. C. • OCTOBER 1969

1. Report No. NASA TM X-1842	2. Government Accession No.	3. Recipient's Catalog No.
4. Title and Subtitle EXPERIMENTAL INVESTIGATION OF DYNAMIC DISTORTION IN A MACH 2.50 INLET WITH 60 PERCENT INTERNAL CONTRACTION AND ITS EFFECT ON TURBOJET STALL MARGIN		5. Report Date October 1969 6. Performing Organization Code
7. Author(s) James E. Calogeras		8. Performing Organization Report No. E-5102
9. Performing Organization Name and Address Lewis Research Center National Aeronautics and Space Administration Cleveland, Ohio 44135		10. Work Unit No. 126-15-02-11-22 11. Contract or Grant No.
12. Sponsoring Agency Name and Address National Aeronautics and Space Administration Washington, D.C. 20546		13. Type of Report and Period Covered Technical Memorandum 14. Sponsoring Agency Code
15. Supplementary Notes		

16. Abstract

An investigation was made in the Lewis 10- by 10-Foot Supersonic Wind Tunnel of dynamic distortion within an inlet and of its effect on the stall margin of a J85-GE-13 turbojet engine. Results indicate that average rms pressure fluctuations of 5 percent of the steady-state total pressure can completely degrade stall margin at certain engine speeds. Vortex generators were much more effective than throat bleed in suppressing dynamic distortion at off-design operating conditions. The presence of the engine appeared to have no effect on either the magnitude or the spatial distribution of dynamic distortion.

17. Key Words (Suggested by Author(s))	18. Distribution Statement
Inlet-engine compatability Dynamic distortion	Unclassified - unlimited

19. Security Classif. (of this report)	20. Security Classif. (of this page)	21. No. of Pages	22. Price*
Unclassified	Unclassified	46	$3.00

*For sale by the Clearinghouse for Federal Scientific and Technical Information Springfield, Virginia 22151

EXPERIMENTAL INVESTIGATION OF DYNAMIC DISTORTION IN A MACH 2.50 INLET WITH 60 PERCENT INTERNAL CONTRACTION AND ITS EFFECT ON TURBOJET STALL MARGIN

by James E. Calogeras

Lewis Research Center

SUMMARY

A wind tunnel investigation was made to determine the amplitude and spatial distribution of dynamic distortion produced in an inlet with 60 percent of the overall supersonic area contraction occurring internally, and to determine the effect of this dynamic distortion on compressor stall margin. The effects of subsonic diffuser vortex generators, inlet throat bleed, and engine presence on dynamic distortion were also investigated. Results showed that compressor stall margin was not seriously reduced by an average rms amplitude of the fluctuating component of total pressure equal to 2 percent of the steady-state total pressure. An increase in this dynamic distortion rms amplitude to 5 percent of the steady-state total pressure could, however, cause complete degradation of the stall margin at certain engine speeds. The use of vortex generators on the cowl and centerbody surfaces was found to be very effective in reducing dynamic distortion over the entire inlet-operating range. A 300-hertz resonance existed at most of the inlet-operating conditions. This resonance originated in the cavities associated with the inlet bypass ports which were placed just upstream of the compressor face station. This resonance had a strong effect on the spatial distribution of high local dynamic distortion lobes. The presence of the engine had no significant effect on either the average magnitude of steady-state and dynamic distortions or their respective spatial distributions.

INTRODUCTION

It has long been recognized that the flow from a supersonic diffuser may have a serious total pressure distortion at the compressor face which can influence engine stall

margin. More recently it has become apparent that total pressure fluctuations at the compressor face can also alter stall margin. A major share of this dynamic distortion appears to originate from the unsteady interaction of the diffuser terminal shock with the inlet boundary layer. This interaction produces localized three-dimensional transients in total pressure at the diffuser exit. The effects of dynamic distortion on compressor stall margin were first observed during wind tunnel tests of the XB-70 propulsion system. A subsequent investigation was made which artificially created distortion dynamics in an altitude engine test facility utilizing a choke point and subsonic diffuser ahead of a turbojet (ref. 1). Shock waves downstream of this choke point interacted dynamically with the duct boundary layer, and the effects of resultant dynamic distortion were determined on the stall margin of a GE-J93 turbojet engine.

Only limited data are presently available (e.g., ref. 2) which define the dynamic distortion that actually exists within an inlet in supersonic flight. Moreover, since the dynamic distortion problem has been recognized, this type of study has not been made in a wind tunnel with a complete inlet and turbojet engine system. Therefore, the present study was undertaken to determine the amplitude and spatial distribution of dynamic distortion produced in a typical supersonic inlet and also to determine the effects of this distortion on compressor stall margin. Some preliminary results are presented in reference 3. This investigation was one part of an overall inlet-engine program which included a detailed optimization of inlet steady-state performance (refs. 4 to 6), an investigation of the dynamic response of the inlet (ref. 7), and an investigation of steady-state inlet-engine interactions (ref. 8). The current study was conducted in the Lewis 10- by 10-Foot Supersonic Wind Tunnel over a Mach number range from 2.0 to 2.8. An axisymmetric mixed-compression inlet designed for Mach 2.5 was mounted to a nacelle in which either a coldpipe-choked plug assembly or a J85-GE-13 turbojet engine could be installed. Both steady-state and dynamic distortion measurements were made using first the coldpipe assembly and then the engine. Engine effects on these parameters were then obtained by comparing them at similar inlet operating conditions. The effects of inlet configuration variables, such as throat bleed and vortex generators, on dynamic distortion were investigated for critical and supercritical inlet operation. The engine was stalled at representative inlet conditions to determine the effect of dynamic distortion on compressor stall margin.

SYMBOLS

b vortex generator height, 1.27 cm

H annular height at diffuser station 2

h	radial distance from centerbody surface
M	Mach number
m/m_0	ratio of local mass flow rate to the captured mass flow rate of a stream tube (at free-stream Mach number) with cross-sectional area equal to the projected cowl lip area
N	engine speed
N^*	rated engine speed, 16 500 rpm
P	total pressure
ΔP	fluctuating component of total pressure
$(P_{max} - P_{min})/\overline{P}$	steady-state distortion parameter
$\Delta\overline{P}_{rms}/\overline{P}$	dynamic distortion parameter
$\dfrac{\left(\dfrac{\overline{P}_3/\overline{P}_2}{W_{corr,2}}\right)_{stall} - \left(\dfrac{\overline{P}_3/\overline{P}_2}{W_{corr,2}}\right)_{nol}}{\left(\dfrac{\overline{P}_3/\overline{P}_2}{W_{corr,2}}\right)_{nol}}$	compressor stall margin
p	static pressure
Δp	fluctuating component of static pressure
R_c	cowl-lip radius, 0.2366 m
T	total temperature
W_{corr}	engine corrected airflow
x	axial distance
Δx	axial distance from spike tip
x_t	axial distance of terminal shock downstream of geometric throat
α	angle of attack
θ	T/288.2 K
θ_l	cowl-lip-position parameter, $\tan^{-1} 1/(\Delta x/R_c)$, deg

Subscripts:

bl	performance bleed

crit critical inlet operation

h local conditions along rake

max maximum

min minimum

nol normal operating line

rms root-mean square value

stall compressor operating point just prior to stall

0 free-stream station

2 diffuser exit (compressor face) station

3 compressor discharge station

Superscript:

$\bar{}$ area weighted average

APPARATUS AND PROCEDURE

Model Details

The model installed in the 10- by 10-Foot Supersonic Wind Tunnel is shown in figure 1. The bump seen in the lower portion of the nacelle was necessary to house the engine accessory package. As illustrated in figure 2, either a coldpipe-choked plug assembly or a J85-GE-13 turbojet engine could be attached to the inlet nacelle. Inlet design details and system optimization studies have been made for this particular inlet and are reported in references 4 to 6. Some of the more pertinent details, however, are illustrated in figures 3(a) and (b). The inlet was an axisymmetric mixed-compression type with 60 percent of the supersonic flow area contraction provided internally. The 12.5° half-angle spike was translated to effect inlet start. At the geometric throat, the centerbody turned sharply from an angle of about 0° to -5.7°, leading to a 1° equivalent conical expansion throat region. The throat region length was four hydraulic radii. Cowl and centerbody boundary-layer bleeds were provided by perforations both fore and aft of the geometric throat. Provisions were also included for installing vortex generators on the cowl and centerbody aft of the throat region. The compressor face station was segmented by three hollow centerbody support struts which extended forward about half the length of the internal portion of the diffuser. Each of the three duct segments contained two bypass cavities. Secondary and overboard airflow was ported from each

of the cavities to provide engine cooling and off-design engine airflow matching, respectively.

Four inlet configurations differing in performance bleed and/or vortex generator locations were used in this investigation. Performance bleed details of the various configurations are presented in figure 3(c). They correspond to near optimum performance bleed (II), about twice that amount of bleed (III), and no bleed downstream of the throat (I). Most bleed variations were made aft of the geometric throat. Note that centerbody bleed was provided at the second oblique shock impingement point but not at the first point. Vortex generator details are presented in figure 3(d). Only centerbody vortex generators were used with bleed configurations II and III, and the combinations are denoted, respectively, configurations IIND' and IIIND'. Bleed configuration I was tested both without generators (configuration I) and with cowl and centerbody generators (configuration IND).

Instrumentation and Dynamic Recording Procedure

Steady-state and dynamic pressure instrumentation at the compressor face station is presented in figure 4. Total pressure recovery and steady-state distortion (defined as the maximum difference between any two total pressures ratioed to the mean total pressure) were measured by the two fixed rakes in the lower right duct segment as viewed from upstream. (These ten-tube rakes consisted of six equal area weighted tubes with additional tubes added at each side of the extreme equal area-weighted tubes in positions corresponding to an 18-tube area-weighted rake.) Profiles presented in reference 6 indicate axial symmetry of the flow at 0° angle of attack; therefore measurements in any of the three duct segments were representative of the entire flow field. In order to measure the fluctuating component of total pressure, subminiature absolute pressure transducers were mounted in rotating rakes cantilevered from the centerbody in both the top and lower left duct segments. The 1.905-centimeter tube length was necessary to protect the transducer diaphragm from particle damage but still was short enough to yield a flat response to at least 1000 hertz. Such a pneumatic system does, however, produce a closed-end organ pipe resonance at approximately 4200 hertz. Additional dynamic instrumentation in the upper duct segment included a fixed single-tube total pressure rake to correlate with those on the rotating rakes and with flush-mounted static pressure transducers on the cowl and centerbody.

The unfiltered fluctuating component of each pressure transducer was recorded on frequency modulated magnetic tape at $7\frac{1}{2}$ inches (19 cm) per second. This tape speed provided flat response to 2500 hertz. In addition, output signals of rotating rake trans-

ducers in the upper duct segment were filtered by first order low-pass filters with a 1000-hertz corner frequency and measured with trms meters. Response characteristics of both the unfiltered and the filtered outputs of the dynamic probes with the 1.905-centimeter tube length are presented in figure 5. Although the filtered signal still contains a significant resonance at 4200 hertz, spectrum analyses of data indicate that the overall contribution to an average rms amplitude of total pressure fluctuation from those frequencies above 1000 hertz was only 10 to 15 percent. At each steady-state operating condition, dynamic data were recorded at the four rotating rake positions shown in figure 4. The average value of the 16 rms measurements of the fluctuating component of total pressure in the upper duct segment was ratioed to the average steady-state recovery pressure. This value was defined as the dynamic distortion level for that particular operating condition. Later comparisons between upper and lower duct dynamic distortion levels indicated insignificant differences for 0° angle-of-attack operation. Hence, for purposes of this report, upper duct segment values of dynamic distortion were assumed representative of the entire compressor face flow field at 0° angle-of-attack conditions.

Steady-state instrumentation at the compressor discharge station is presented in figure 6.

Test Procedure

The initial phase of this investigation was concerned with measuring dynamic distortion for the various inlet configurations with the coldpipe assembly. For each configuration, an inlet-engine match point was defined at a compressor face corrected airflow of about 16.0 kilograms per second. This corresponded to the airflow requirement of a J85-GE-13 turbojet engine at a corrected speed of 86.5 percent of the rated speed. Ejector secondary bypass flow at the match point was about 3 percent of the captured mass flow for each configuration. The terminal shock was positioned approximately in the middle of the throat region for configuration IIND' at the match point. This required an overboard bypass of about 2 percent of the captured mass flow. Because of the increased performance bleed of configuration IIIND', the terminal shock was located at the downstream end of the throat region for match point operation. In this case the overboard bypass was closed. Because configurations I and IND had no bleed in the throat region, the terminal shock could not be stabilized in that region. For these configurations, then, the only stable terminal shock locations in the vicinity of the throat region were either just upstream or downstream of the region. When the terminal shock was positioned upstream of the geometric throat, it caused a separation extending into the supersonic diffuser section which increased the bleed in that region as discussed in

references 4 and 6. This provided a stable shock structure. The upstream position was used in setting the engine match point for both configurations I and IND. Match point overboard bypass flow was about 2 percent of the captured mass flow for configuration I and about 6 percent for configuration IND.

Several other inlet operating conditions were investigated for each of the inlet configurations. At the inlet design Mach number and contraction ratio and at 0^{o} angle of attack, data were taken for various overboard bypass flows at the match compressor face corrected airflow. Data were also taken at various compressor face corrected airflows by varying the choked plug area while keeping bypass area at the original match point setting. Undercontracted inlet geometries, angles of attack, and off-design Mach number operations were investigated at the match corrected airflow.

The second phase of this investigation included both a sea-level static and a wind tunnel engine program. The static test was limited to obtaining a compressor stall line calibration with air supplied by a bellmouth. Wind tunnel tests determined not only the effect of dynamic distortion on compressor stall margin but also the effect, if any, of the presence of the engine on both steady-state and dynamic distortion. The procedure used to obtain compressor stalls was the same for both programs. Starting at a compressor pressure ratio in the vicinity of a standard engine normal operating line, incremental reductions of exhaust nozzle area were made. These reductions rematched the compressor to the turbine at higher compressor pressure ratios. Engine speed was held constant throughout this procedure by manually biasing the throttle. Steady-state and dynamic data were recorded at each point on a corrected speed line until compressor stall occurred. The equilibrium operating point recorded just prior to stall was termed the stall point and was used in the definition of compressor stall margin. This procedure was repeated at different speeds in the static test stand to calibrate the stall line. In the wind tunnel, the above stall procedure was repeated at different inlet-operating conditions and engine speeds to determine the effect on compressor stall margin. In order to avoid overtemperaturing the turbine, a reduced-area first-stage turbine stator was used to force the compressor to operate at a higher than normal pressure ratio for each turbine inlet temperature. Turbine stator area was reduced by 26 percent for sea-level tests and by 14 percent for wind tunnel tests. Compressor interstage bleed, mechanically linked to the inlet guide vanes, was scheduled linearly from full closed at 90 percent corrected speed to full open at 76 percent corrected speed for both engine programs. This schedule corresponds to the maximum allowable bleed closure for safe engine operation and was required to obtain many of the stalls at engine corrected speeds below 94 percent. The normal schedule actuates the bleed valves between corrected speeds of 94 and 80 percent. Exhaust nozzle blockage plates were required to force compressor stalls at engine speeds below 90 percent of rated speed.

RESULTS AND DISCUSSION

Coldpipe Test Results

Performance of the various inlet configurations is presented in figure 7 for Mach 2.50, 0° angle-of-attack operation at the design inlet contraction ratio. Data are shown for various bypass flows at the match compressor face corrected airflow (squares) and various compressor face corrected airflows at the original match point bypass flow (circles). Dynamic distortions for configuration IIND', presented in figure 7(a), range from about 2 percent of the steady-state total pressure at the match point pressure recovery of 0.91 to about 6 percent at 0.73 total pressure recovery. Between recoveries of 0.80 and 0.77, large bypass flows remove low-energy air from the cowl, resulting in lower steady-state and dynamic distortions. At recoveries below 0.77, however, large bypass flows cause flow separation from the centerbody. Results for configuration IIIND' presented in figure 7(b) indicate that increased throat bleed had little effect in reducing steady-state or dynamic distortions at comparable pressure recoveries. The matched condition for this configuration was somewhat more supercritical than that of the other configurations tested. This was necessary because the additional performance bleed flow, even with no overboard bypass, left insufficient inlet flow to meet engine requirements at critical inlet operation. Results for configuration I presented in figure 7(c) are indicative of the relatively high levels of distortion produced when vortex generators and subsonic diffuser section bleed were absent. Dynamic distortions of this configuration were 50 to 100 percent higher than those of configuration IIND' at comparable total pressure recoveries. Results for configuration IND are presented in figure 7(d). Although some loss in peak total pressure recovery was caused by the addition of cowl and centerbody vortex generators, dynamic distortions were lowest of all configurations tested at comparable pressure recoveries. Furthermore, steady-state distortions were reduced to values of about 0.12 or less throughout the entire operating range investigated.

Undercontracted inlet performance typical of inlet operation during restart at Mach 2.5 for configurations IIND', IIIND', I, and IND are presented in figures 8(a) to (d), respectively. All data are for the matched engine corrected airflow of 16.0 kilograms per second. At started inlet minimum stable mass-flow conditions, none of the configurations produced distortions so high as to rule out the possibility of engine operation. Both steady-state and dynamic distortions did, however, increase rapidly with bypass flow. As reported in reference 6, an asymmetric boundary-layer separation phenomenon existed on the spike surface during unstarted inlet operation for spike positions from design ($\theta_l = 26.6^{\circ}$) to midway to restart ($\theta_l = 23.4^{\circ}$). The resultant unstarted steady-state distortions had large circumferential components. Such distortions could

not be accurately determined with only the two total pressure rakes used in this investigation and, hence, are omitted from figure 8. Values of steady-state distortion at similar unstarted conditions were obtained from reference 6 and are presented later in figure 22.

The effect of off-design Mach number on the performance of inlet configurations IIND', I, and IND is presented in figures 9(a) to (c), respectively. As evidenced in figure 9(c), cowl and centerbody vortex generators were instrumental in maintaining fairly low steady-state and dynamic distortion levels even at the Mach 2.79 overspeed condition. At Mach 2.79, throat Mach number was about 1.60 compared to 1.24 at the inlet design Mach number.

The variation of total pressure recovery and of steady-state and dynamic distortion with terminal shock position is presented in figure 10 to further emphasize the effectiveness of the vortex generator configuration used on configuration IND. Terminal shock location was estimated from an axial row of cowl static pressure taps. Even without throat bleed, the measured total pressure recoveries were higher with this configuration than those of the other configurations when compared at similar terminal shock locations downstream of the vortex generator station.

Typical traces of some compressor face dynamic probes are presented in figure 11. A dominant frequency of approximately 300 hertz can be noted in each trace. All inlet configurations exhibited this resonance during operation with the terminal shock near the throat. As the shock was pulled downstream, the periodicity of the fluctuating pressures became more or less apparent depending on the configuration and whether bypass or engine flow was increased. The coherency of the resonance is least apparent in figure 11(d), which has a ratio of peak-to-peak amplitude to the rms value of 5.8 compared with the ratio of 4.6 of figure 11(c). Some idea of the randomness of the signals can be envisioned from the fact that for a pure sinusoidal signal, the peak-to-peak to rms ratio is 2.838; for a normal random signal, the ratio is 6.0. Since the resonant amplitude varied with inlet operating condition, however, its relative portion of the total dynamics has not yet been determined. Tests subsequent to the investigation reported herein indicated that the resonance was generated by the cavities associated with each bypass door. These cavities acted as resonators with the energy source being the airflow in the main duct. Use of an annular dual-vane cascade at the entrance to each cavity, as described in reference 3, successfully decoupled the cavity from the main duct and eliminated the resonance.

Steady-state and dynamic rake profiles of inlet configurations IIND', IIIND', I, and IND are presented in figures 12(a) to (d), respectively. Profiles are shown for match point operation as well as for supercritical points obtained both by choked exit plug variation (engine overspeed) and by bypass variation. Profiles of configurations IIND' and IIIND' are characterized by high steady-state pressures toward the centerbody and high dynamic pressures toward the cowl for supercritical conditions, particularly with large

bypass flows. This is apparently the result of vortex generator action on the centerbody only. Without vortex generators, configuration I exhibits higher steady-state pressures toward the cowl, whereas dynamic pressures appear to show no geometric preference. With cowl and centerbody generators, configuration IND has uniform steady-state and dynamic total pressure profiles.

Steady-state and dynamic rake profiles for configurations IIND' and IND are presented in figures 13 and 14, respectively. These figures are presented to further illustrate profile transition as the terminal shock traverses downstream.

Total pressure recovery and dynamic distortion contours for configurations IIND', IIIND', I, and IND are presented in figures 15, 16, 17, and 18, respectively. Included in these figures are contours obtained at match and supercritical operating conditions, undercontracted inlet conditions, and off-design Mach number conditions. Data from the upper duct segment were used exclusively in preparing the dynamic pressure contours, whereas the steady-state pressure contours were derived from two fixed rakes in one of the lower duct segments. No consistent correlation is evident in these figures between steady-state and dynamic distortion. A close inspection of these figures does tend, however, to illustrate some general characteristics of the dynamic distortion contours. For example, in all of the cases presented, the highest-valued dynamic distortion lobe is never more than twice the amplitude of the lowest-valued contour. Furthermore, in instances of relatively high steady-state distortion such as presented in figures 15(b), 16(b), and 17(c), regions of the highest dynamics appear localized between high and low steady-state pressure regions. Finally, in several of the remaining cases, the highest-valued local dynamic distortion lobes occur near the cowl surface just under each of the two bypass cavities in the upper duct segment. Apparently the spatial distribution of dynamic distortion was influenced by the resonances associated with these cavities.

Steady-state and dynamic total pressure contours are presented in figure 19 for supercritical operation of configuration IIND' at angles of attack of 0° (fig. 19(a)), and 4.8° (fig. 19(b)). Steady-state contours were obtained from previously unpublished data of reference 6. Note that at positive angle of attack the highest dynamics appear to be crowded along the upper support struts, whereas the lowest total pressure recovery region is along the bottom strut. This particular angle of attack was slightly less than the inlet unstart angle for Mach 2.58.

Inlet Performance with Engine Installed

Steady-state and dynamic performance of the inlet coupled to the J85-GE-13 turbojet engine is presented in figure 20 for Mach 2.50, 0° angle-of-attack operation at the design contraction ratio. Results are shown for all of the inlet configurations except

IIIND'. To obtain these data, the engine was run at or as close to the sea-level static normal operating line as was possible with the reduced area turbine diaphragm. Coldpipe results for each configuration are also reproduced in this figure for ease of reference. Results indicate that the presence of the engine had little or no effect on the average levels of either steady-state or dynamic distortion. Since dynamic distortion is used in this report as a time-averaged parameter, this does not necessarily imply that engine presence would have no effect on an instantaneous distortion.

Steady-state and dynamic total pressure profiles are presented in figure 21 for configurations IIND', I, and IND at supercritical operating conditions. Profiles obtained from the coldpipe test at identical or near-identical operating conditions are presented for comparison. Again no significant effects of engine presence on either steady-state or dynamic rake profiles are indicated in this figure.

An unstart-restart cycle for configuration IIND' during peak recovery operating conditions is presented in figure 22. The sharp increase in steady-state distortion shown at a pressure recovery of 0.615 was due primarily to the asymmetric boundary-layer separation phenomenon previously mentioned in the discussion of figure 8. This separation resulted in relatively large circumferential distortions at the compressor face. Because the two steady-state total pressure rakes used in this investigation could not accurately determine total pressure recovery or steady-state distortion when confronted with large circumferential distortions, data from reference 6 were used to determine these parameters. Compressor face instrumentation used in the investigation reported in reference 6 included two steady-state rakes in each of the lower duct segments and three rakes in the upper duct segment. At the Mach 2.50 design inlet contraction ratio, the inlet could not be stabilized during unstarted operation. This problem, coupled with the asymmetric boundary-layer separation phenomenon, precluded any attempt to operate the engine in the unstarted inlet mode at spike positions (θ_l) greater than 22.8°. Of that portion of the restart cycle shown with engine operation, dynamic distortion was found to be highest at the point just subsequent to inlet restart. However, no compressor stalls were encountered at this condition or any of the other engine operation points shown in the cycle.

Results of the sea-level static test to determine the undistorted inflow stall line of the particular engine used in this investigation are presented in figure 23. The normal operating line shown was used as the base in computing stall margins for these static test stalls and for those obtained in the wind tunnel. The datum points connected by the stall line are not extrapolated; they are equilibrium points obtained just prior to stall.

The stall points obtained with inlet configuration IND in the wind tunnel are presented on a compressor map in figure 24. In order to better isolate the effects of dynamic distortion on stall margin from the effects of steady-state distortion, the majority of points used in the summary curves of figure 25 were obtained with this inlet configu-

ration. Dynamic distortion values for this configuration varied from 0.015 to 0.049; steady-state distortions for the same points were small and relatively constant. Because of the particular definition of stall margin used in this report, the computed stall margin of configuration IND at a corrected speed of 99.5 percent is about equal to the computed stall margin for undistorted inflow at a corrected speed of 100.3 percent (refer to fig. 23). While the stall point of configuration IND at 99.5 percent corrected speed obviously falls below the undistorted inflow stall line, it occurs at an appreciably smaller value of corrected airflow than does the 100.3 percent corrected speed point for the undistorted inflow case. The apparent discrepancy in computed stall margins for these two points then arises because of the rapid convergence of the undistorted inflow stall line and the normal operating line (used as a reference in defining stall margin) as corrected airflow increases from the value at the 99.5 percent corrected speed point of configuration IND.

Summary curves of stall margin against engine corrected speed for various levels of dynamic distortion are presented in figure 25. By defining stall margin in the manner of this figure, any difference between the value of engine corrected airflow at stall and the value at the normal operating line was accounted for. The undistorted inflow curve was faired from the results of figure 23. The cusp shown in all of the stall margin fairings was probably related to the modified interstage bleed schedule which called for full-bleed closure at an engine corrected speed of 90 percent rather than the normal value of 94 percent. Since the inlet guide vanes are mechanically linked to the interstage bleed schedule, the modified schedule called for full-open guide vanes at the 90 percent corrected speed condition. Closing the interstage bleed and opening the inlet guide vanes both tend to further load the front stages of the compressor, making these stages more sensitive to distortion.

Because a larger turbine diaphragm than that used in the sea-level static test was used in the wind tunnel test, the compressor could not always be stalled before the turbine inlet temperature limit was reached. Such temperature limit points, however, were still used in preparing this figure. A stall margin computed for each of these points was considered a minimum for that respective level of dynamic distortion. Steady-state distortion for all but two of the points was 0.10 or less. For purposes of further discussion, these distortions are assumed to have no significant effect on compressor stall margin. This is probably not absolutely true, and the measured compressor inlet conditions are presented in later figures for comparison. Nevertheless, the stall margin fairings presented are intended primarily to show qualitative trends of stall margin degradation with dynamic distortion. As such, the results of this figure indicate that while a dynamic distortion level of 0.02 can be tolerated, a level of 0.05 can completely degrade stall margin at certain engine speeds. Steady-state and dynamic distortion values for each of the distorted inflow points of figure 25 are presented in table I.

TABLE I. - DISTORTION VALUES FOR STALL AND TEMPERATURE

LIMIT POINTS OF FIGURE 24

Corrected speed	Stall margin	Point	Configuration	Steady-state distortion	Dynamic distortion
86.4	0.286	Temperature limit	IIND'	0.072	0.016
86.4	.262	Temperature limit	IIND'	.062	.017
86.5	.165	Stall	IND	.082	.035
87.0	.304	Temperature limit	IND	.058	.015
87.9	.311	Temperature limit	IIND'	.071	.020
88.3	.211	Stall	I	.177	.044
88.3	.189	↓	I	.172	.037
89.9	.258	↓	IND	.071	.019
90.0	.263	↓	IND	.058	.018
90.0	.252	↓	IIND'	.089	.022
90.1	0	↓	IND	.098	.042
92.3	.263	Temperature limit	IND	.078	.020
92.4	.200	Stall	IND	.050	.028
92.5	.249	Temperature limit	IND	.077	.019
92.5	.129	Stall	IIND'	.100	.031
93.7	.202	Temperature limit	IIND'	.071	.026
93.7	.201	Temperature limit	IIND'	.044	.031
94.8	.194	Stall	IND	.092	.028
95.0	.110	Stall	↓	.073	.044
95.1	.185	Temperature limit	↓	.066	.031
99.0	.139	Temperature limit	↓	.078	.049
99.5	.109	Stall	↓	.048	.045

Mention should now be made of the procedure used in obtaining dynamic distortion values at points just prior to stall or points of limited turbine inlet temperature. As previously mentioned, dynamic distortion by definition required averaging the rms levels of four radial dynamic total pressure probes at each of four circumferential stations. To minimize tunnel operating time, this procedure could not be followed at each of the several datum points recorded in search of the stall point at a given engine speed. Consequently, dynamic distortion was measured for each engine corrected speed only at those points on a compressor map which corresponded to the normal operating line. As data were taken at higher compressor pressure ratios for each engine corrected speed, the dynamic rotating rake was kept in position 4 of figure 4. At a given speed, however, raising the compressor pressure ratio from its normal operating line level to its stall value generally tended to lower engine corrected airflow. When this occurred, overboard bypass was increased to maintain a constant terminal shock position. The net effect was to hold the average total pressure reasonably close between points of stall or turbine temperature limits and points along the normal operating line. Any slight

change in the average level of dynamic distortion between two such points on a compressor map was then accounted for by considering the slight changes in total pressure recovery and engine mass flow and using the results of figure 20.

Steady-state and dynamic distortion rake profiles are presented in figure 26 for each of the distorted inflow stall points of figure 25. For each of the stall point profiles, normal operating line profiles are presented for comparison. Only figures 26(g) and (i) indicate rather large differences in the average total pressure levels. The higher stall point pressures occurring at these conditions indicate that insufficient bypass flow was used to hold terminal shock position constant. Of the other parts of figure 26, most show slightly higher steady-state pressures at stall, especially toward the cowl. Dynamic distortions at stall for these conditions would be correspondingly less than that measured at the normal operating line. Exceptions to this trend appear in figures 26(k) and (l), where steady-state pressures are slightly lower and dynamic pressures slightly higher at stall.

SUMMARY OF RESULTS

A wind tunnel investigation was made to determine (1) the magnitude and spatial distribution of dynamic distortion produced in a Mach 2.50 design inlet with 60 percent internal contraction; and (2) the effect of this dynamic distortion on compressor stall margin. Any effect that the presence of the engine might have on dynamic distortion was determined by comparing results from an inlet-engine combination to those obtained with the inlet connected to a coldpipe-choked plug assembly. The effects of inlet configuration variables, such as throat bleed and vortex generators, on dynamic distortion were investigated for critical and supercritical inlet operation. The particular engine used in this investigation was a J85-GE-13 turbojet. The investigation was conducted at Mach numbers from 2.02 to 2.79. The following results were obtained:

1. Inlet-produced dynamic distortion, defined as the average rms amplitude of the fluctuating component of total pressure ratioed to the average steady-state total pressure, seriously deteriorated compressor stall margin. Results indicate that while a dynamic distortion level of 0.02 can be tolerated, particularly at high engine corrected speeds, a level of 0.05 can completely degrade stall margin at certain engine speeds.

2. Dynamic distortion ranged from 2 percent of the steady-state total pressure at a critical pressure recovery of 0.91 to about 6 percent at a recovery of 0.73 for a reference inlet configuration with centerbody vortex generators and a limited amount of bleed both forward and aft of the geometric throat. Increasing this bleed was ineffective in reducing dynamic distortion. With bleed in only the supersonic diffuser section and no vortex generators, dynamic distortions were 50 to 100 percent higher than those meas-

ured with the reference inlet configuration at comparable total pressure recoveries. By adding vortex generators to cowl and centerbody surfaces, even with only supersonic diffuser section bleed, dynamic distortions were reduced below those of all other configurations at comparable recoveries. Although the peak recovery was somewhat less with this vortex generator configuration, steady-state distortions were also reduced to values of 0.12 or less throughout the operating range investigated.

3. Each configuration exhibited a resonance at about 300 hertz when the terminal shock was in the vicinity of the throat. The resonant amplitude varied with inlet-operating condition, however; and its relative portion of the total dynamics has not been determined.

4. In instances of relatively high steady-state distortions, regions of the highest dynamic pressures generally appear localized between high and low steady-state pressure regions. In several other instances, the spatial distribution of the highest-valued local dynamic distortion lobes appeared to be influenced by the resonances associated with bypass door cavities.

5. Engine presence was found to have no effect on either the average magnitude of steady-state distortion and dynamic distortion rms amplitude or on the spatial distribution of these parameters. Since dynamic distortion is used in this report as a time-averaged parameter, this does not necessarily imply that engine presence would have no effect on an instantaneous distortion.

Lewis Research Center,
National Aeronautics and Space Administration,
Cleveland, Ohio, June 11, 1969,
126-15-02-11-22.

REFERENCES

1. Kimzey, W. F.: An Investigation of the Effects of Shock-Induced Turbulent Inflow on a YJ93-GE-3 Turbojet Engine. ARO, Inc. (AEDC-TR-66-198, DDC No. AD-377312L), Nov. 1966.

2. Coltrin, Robert E.; and Mitchell, Glenn A.: Preliminary Investigation of Distortion Dynamics in a Mach 3 Mixed-Compression Inlet. NASA TM X-1706, 1968.

3. Coltrin, Robert E.; and Calogeras, James E.: Supersonic Wind Tunnel Investigation of Inlet-Engine Compatibility. Presented at the AIAA Propulsion Joint Specialist Conference, Colorado Springs, Colo., June 9-13, 1969.

4. Cubbison, Robert W.; Meleason, Edward T.; and Johnson, David F.: Effect of Porous Bleed in a High-Performance Axisymmetric, Mixed-Compression Inlet at Mach 2.50. NASA TM X-1692, 1968.

5. Sanders, Bobby W.; and Cubbison, Robert W.: Effect of Bleed-System Back Pressure and Porous Area on the Performance of an Axisymmetric, Mixed-Compression Inlet at Mach 2.50. NASA TM X-1710, 1968.

6. Cubbison, Robert W.; Meleason, Edward T.; and Johnson, David F.: Performance Characteristics From Mach 2.58 to 1.98 of an Axisymmetric Mixed-Compression Inlet System With 60-Percent Internal Contraction. NASA TM X-1739, 1969.

7. Wasserbauer, Joseph F.: Dynamic Responses of a Mach 2.5 Axisymmetric Inlet With Engine of Cold Pipe and Utilizing 60-Percent Supersonic Internal Area Contraction. NASA TN D-5338, 1969.

8. Coltrin, Robert E.; and Choby, David A.: Steady-State Interactions from Mach 1.98 to 2.58 Between a Turbojet Engine and an Axisymmetric Inlet With 60-Percent Internal Area Contraction. NASA TM X-1780, 1969.

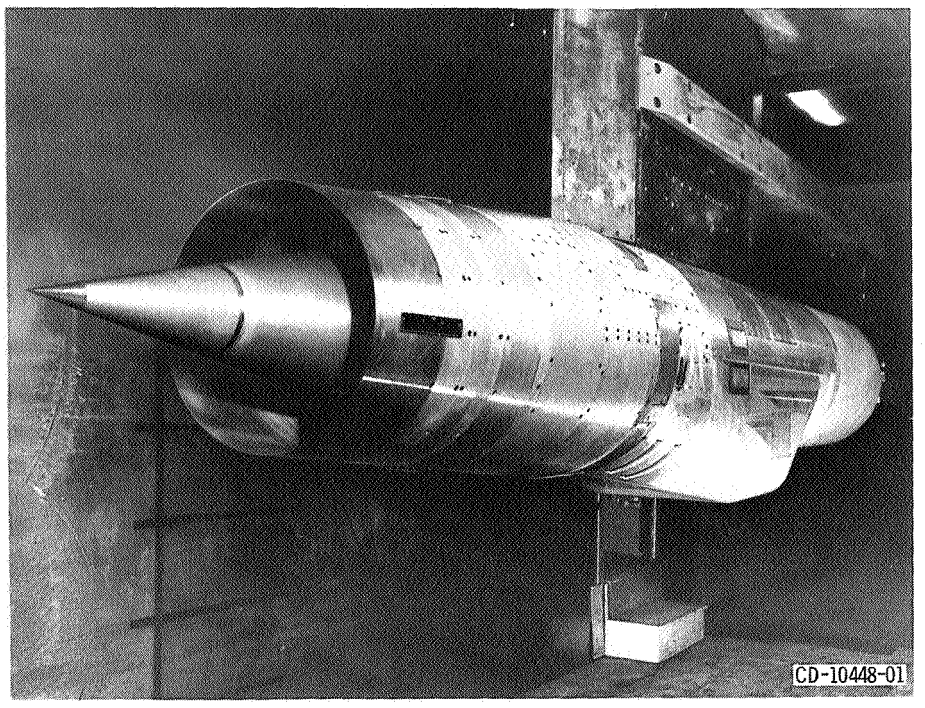

Figure 1. - Model installed in 10- by 10-Foot Supersonic Wind Tunnel.

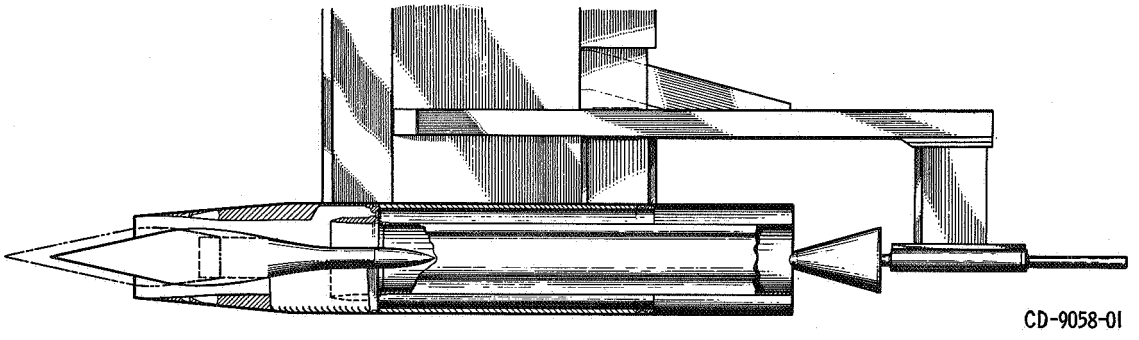

(a) Inlet-coldpipe assembly.

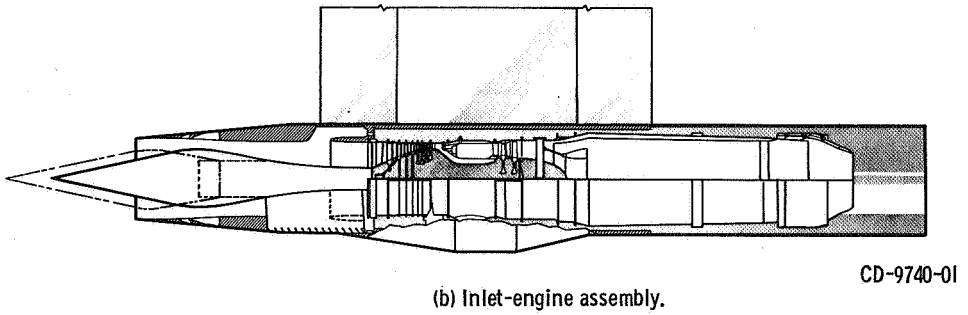

(b) Inlet-engine assembly.

Figure 2. - Nacelle cutaway illustrating both coldpipe and J85-GE-13 turbojet engine installation.

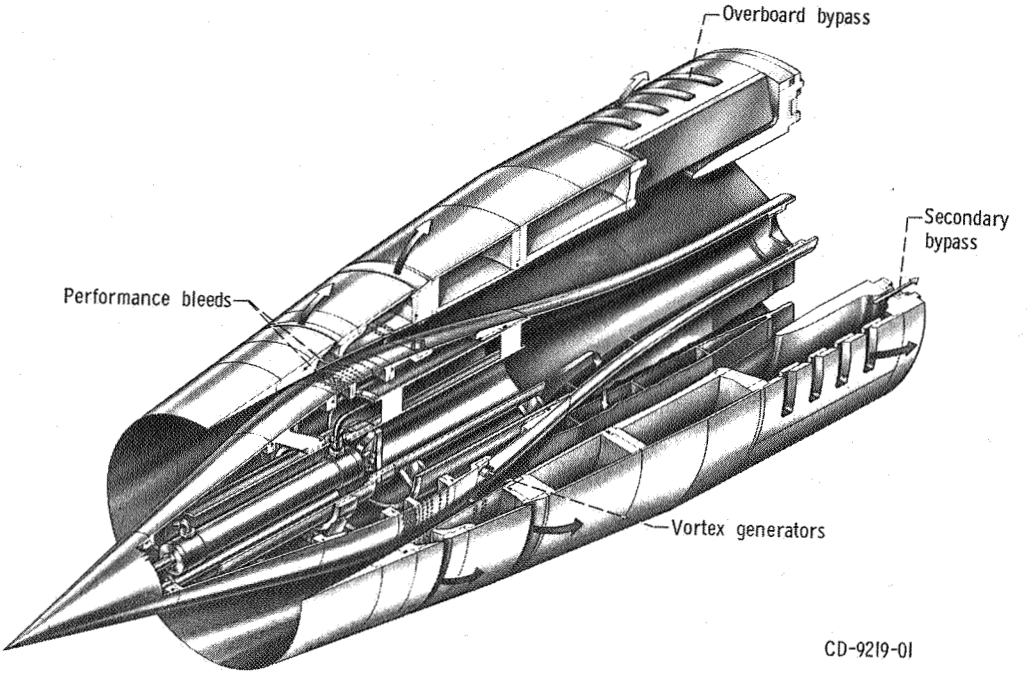

(a) Inlet cutaway.

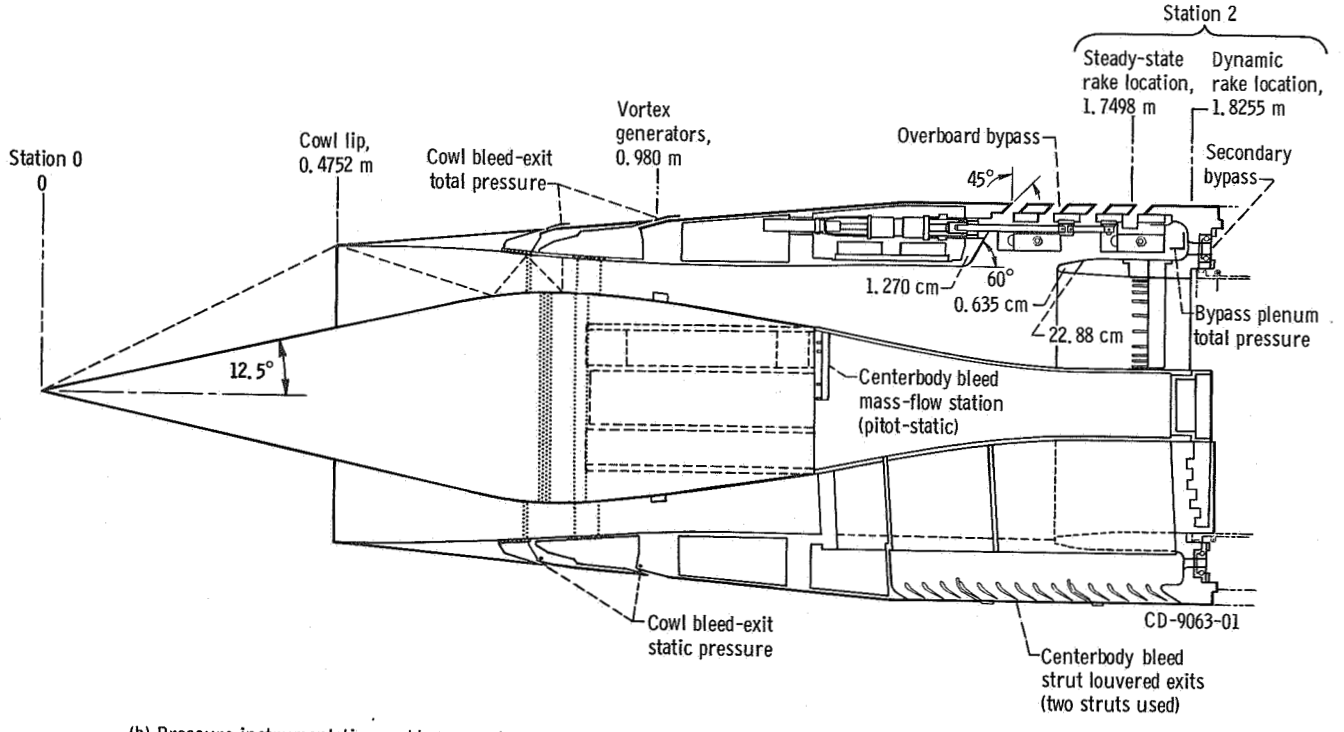

(b) Pressure instrumentation and bypass entrance dimensions. (All stations are referenced to Mach 2.50 centerbody location.)

Figure 3. - Model details.

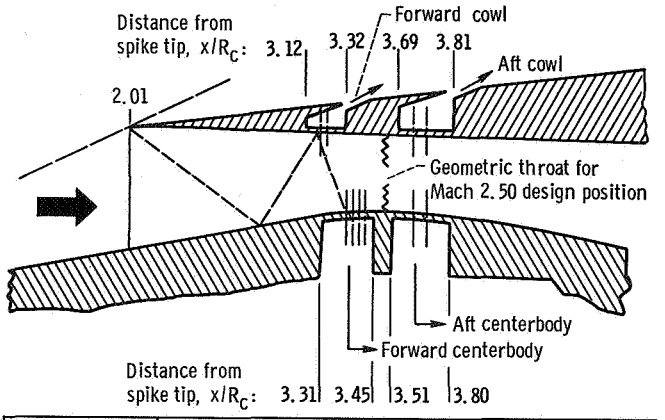

Configuration	Bleed[a]			
	Forward cowl	Aft cowl	Forward centerbody	Aft centerbody
II	○○	◑ ◑	○○○◑	◑ ◑
III	○○	○ ○	○○○○	○ ○
I	○○	● ●	○○○◑	● ●

[a] ○ Row open
◑ Row half open
● Row closed

(c) Performance bleed details for various inlet configurations. (All stations are referenced to Mach 2.50 centerbody location. All bleed holes are 0.3175 cm in diameter.)

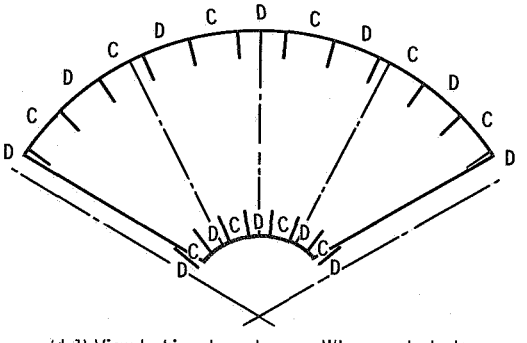

(d-1) View looking downstream. When centerbody generators only are used, configuration is denoted ND'; when both cowl and centerbody generators are used, configuration is denoted ND.

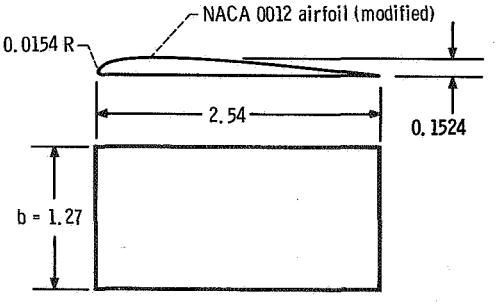

(d-2) Generator details. (All dimensions are in centimeters.)

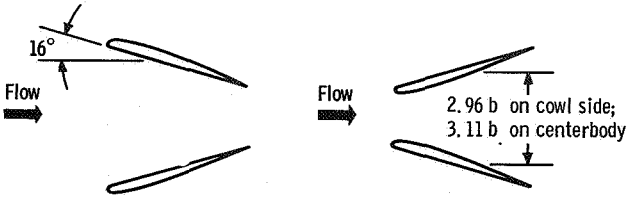

(d-3) Generator orientation.

(d) Vortex generator details.

Figure 3. - Concluded

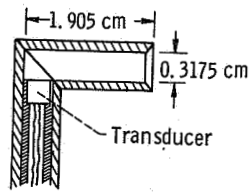

Section A-A (typical through rake only)

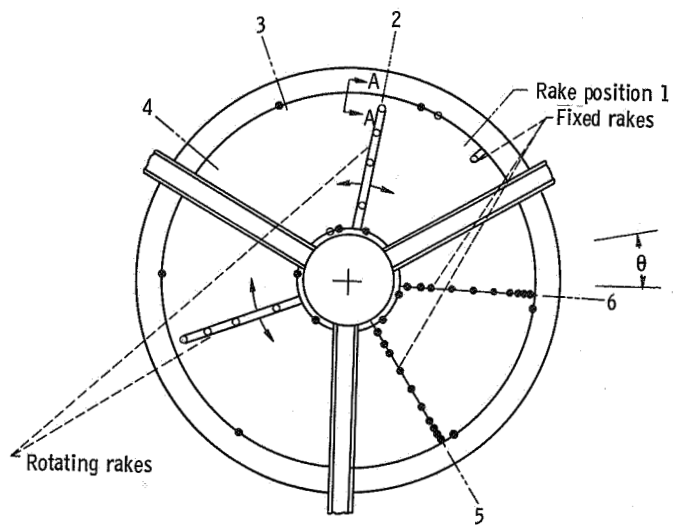

View looking downstream

Rake position	θ, deg
1	50
2	80
3	110
4	140
5	302.5
6	357.5

Figure 4. - Steady-state and dynamic pressure instrumentation at compressor face. (Open symbols denote dynamic pressure instrumentation; solid symbols denote steady-state pressure instrumentation.)

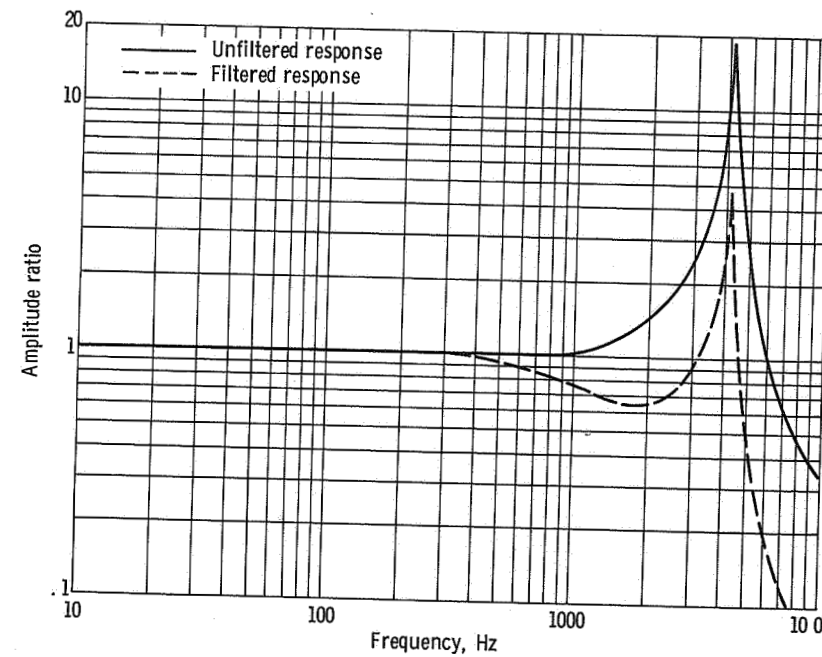

Figure 5. - Frequency response characteristics of dynamic total pressure probes.

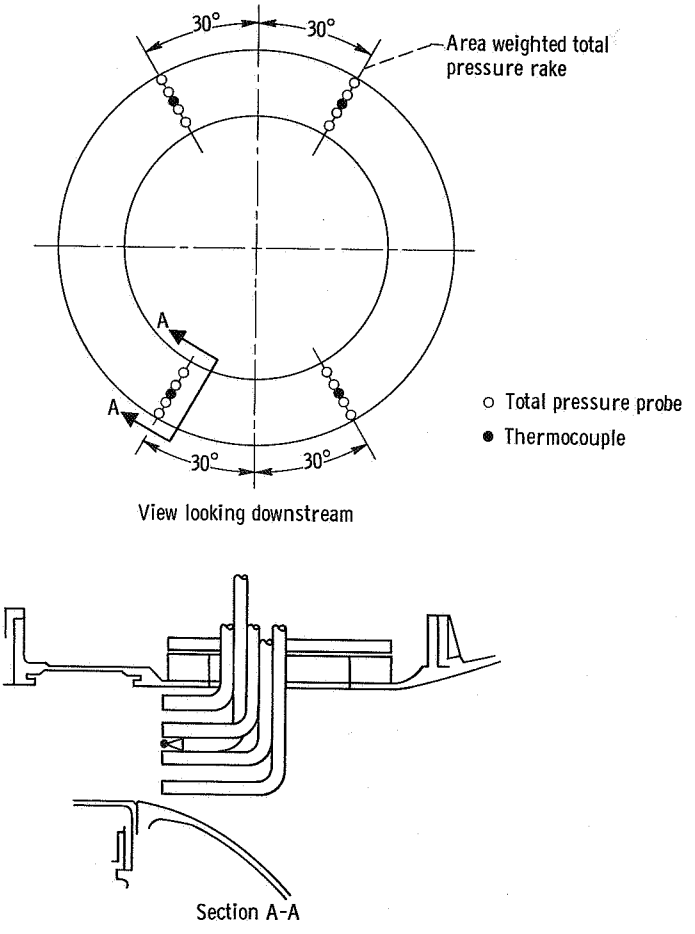

Figure 6. - Compressor discharge instrumentation.

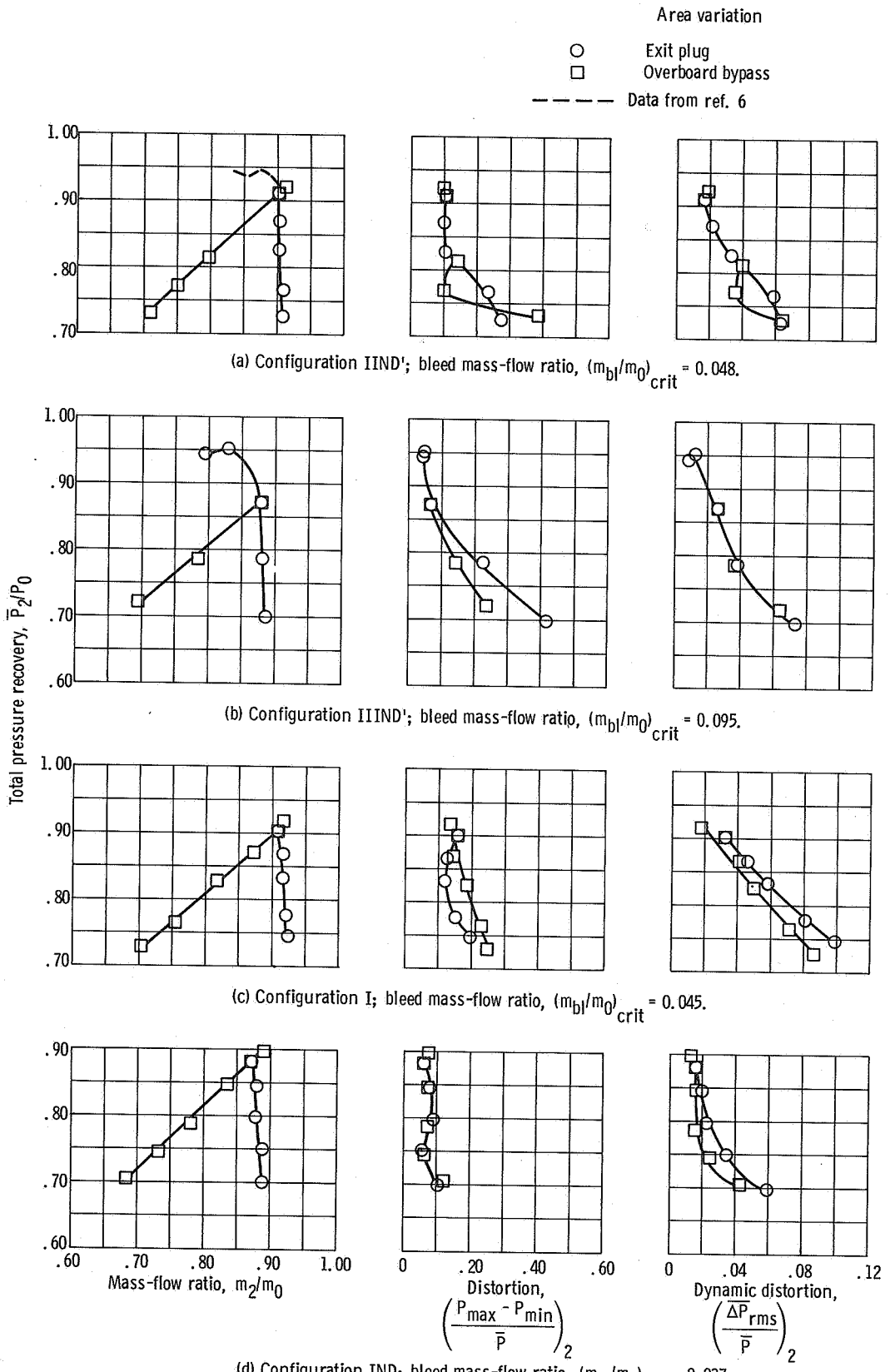

(a) Configuration IIND'; bleed mass-flow ratio, $(m_{bl}/m_0)_{crit} = 0.048$.

(b) Configuration IIIND'; bleed mass-flow ratio, $(m_{bl}/m_0)_{crit} = 0.095$.

(c) Configuration I; bleed mass-flow ratio, $(m_{bl}/m_0)_{crit} = 0.045$.

(d) Configuration IND; bleed mass-flow ratio, $(m_{bl}/m_0)_{crit} = 0.037$.

Figure 7. - Steady-state and dynamic inlet performance at Mach 2.50; angle of attack, 0°; coldpipe tests.

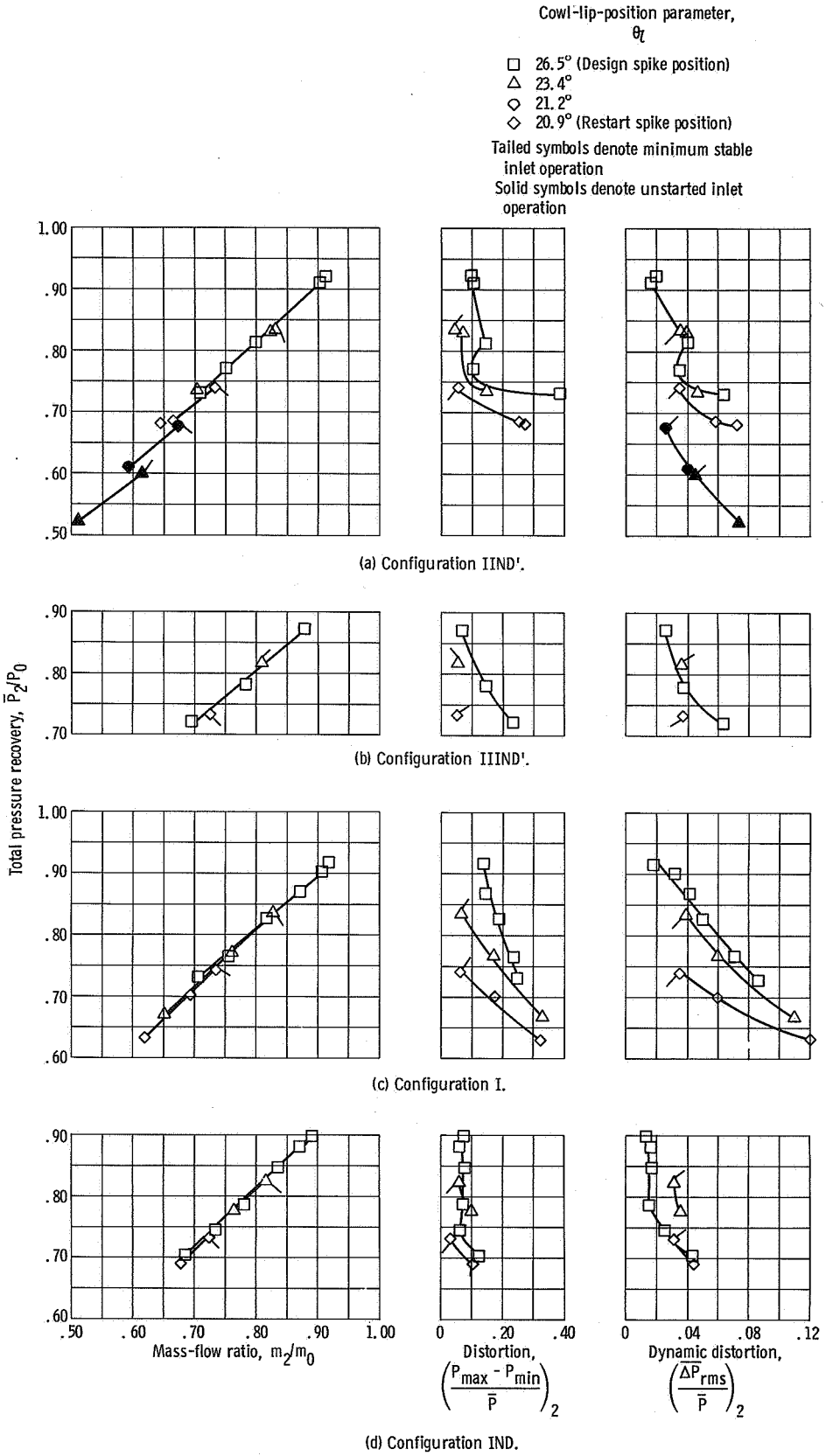

Figure 8. - Effect of undercontracted inlet operation on steady-state and dynamic inlet performance at Mach 2.50; angle of attack, 0°; coldpipe test; match corrected airflow.

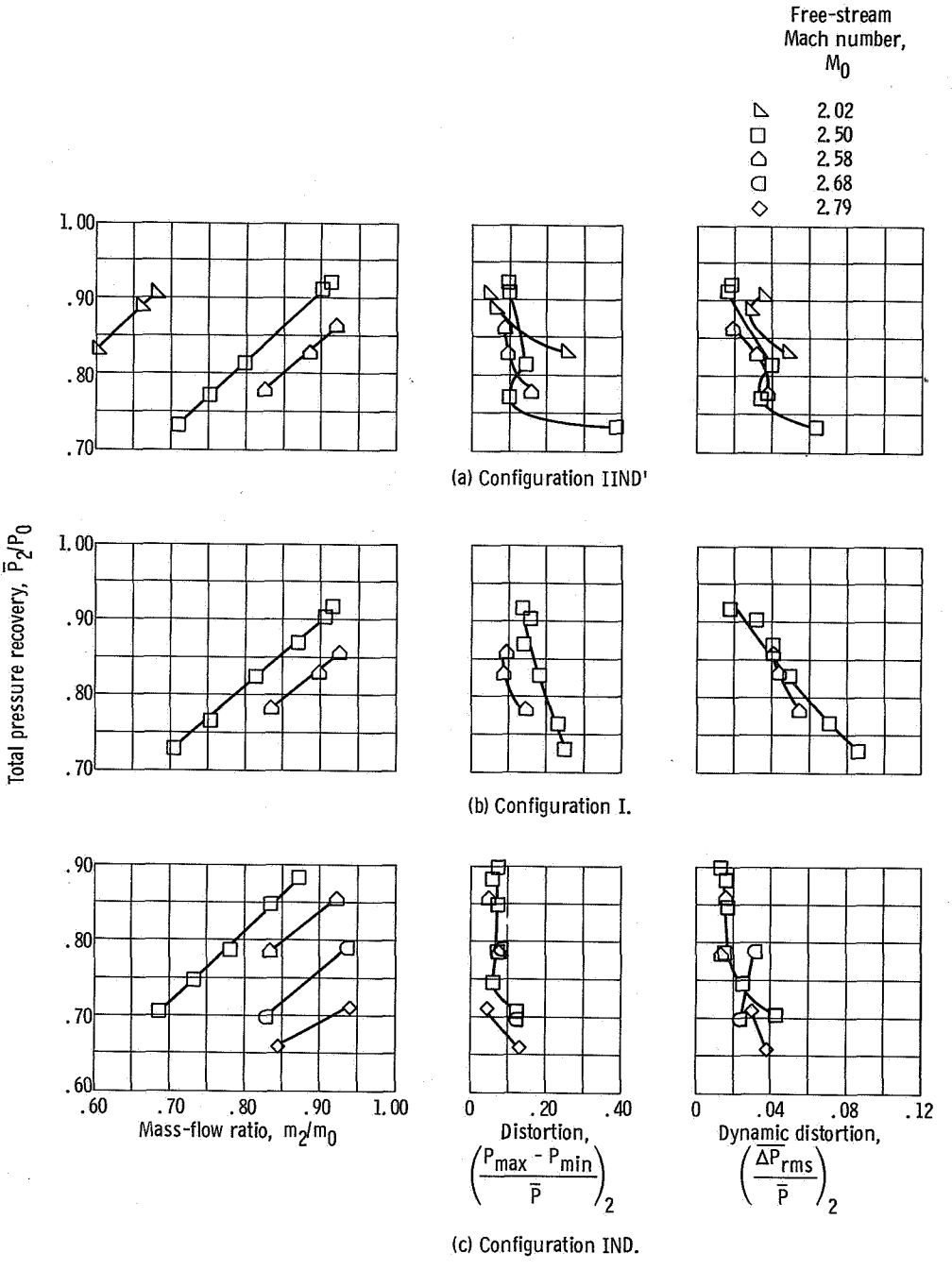

(a) Configuration IIND'

(b) Configuration I.

(c) Configuration IND.

Figure 9. - Effect of free-stream Mach number variation on steady-state and dynamic inlet performance; angle of attack, 0°; coldpipe test.

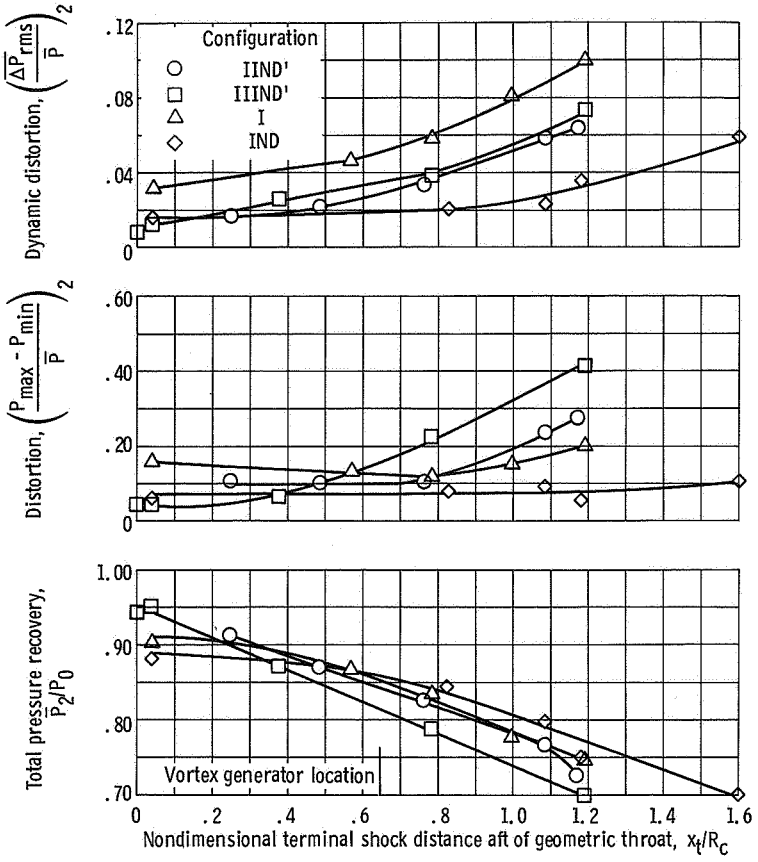

Figure 10. - Variation of steady-state and dynamic inlet performance with terminal shock position at Mach 2.50; angle of attack, 0°; exit plug area variation; coldpipe test.

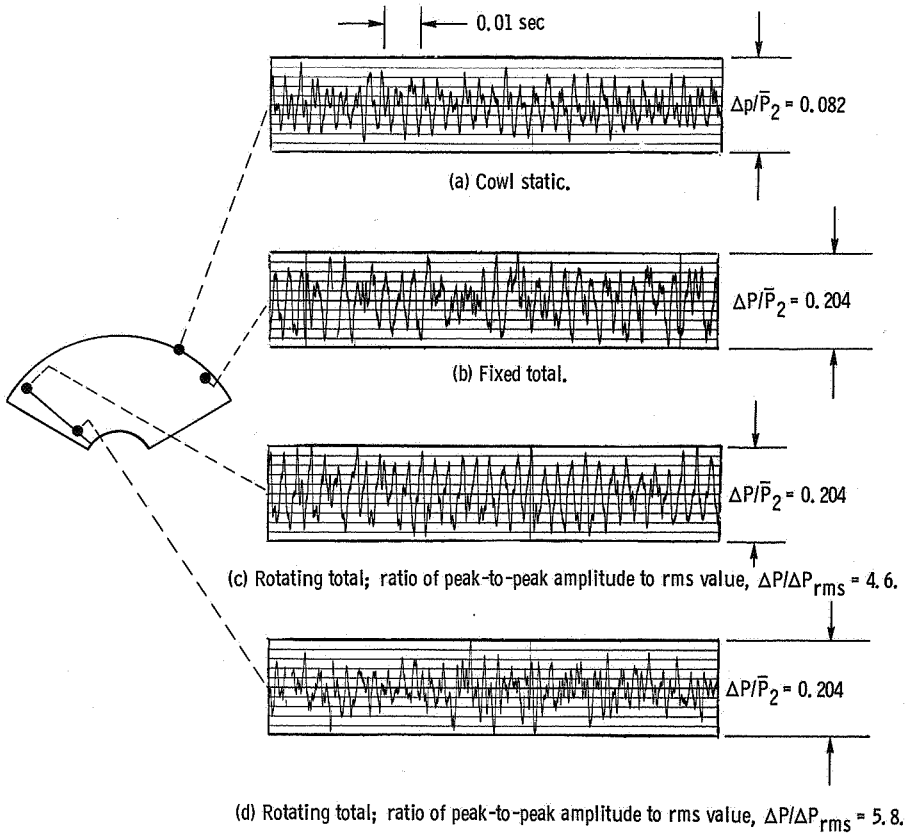

Figure 11. - Typical trace of compressor face pressure fluctuations; inlet configuration, IND; free-stream Mach number, 2.50; mass-flow ratio, 0.889; total pressure recovery, 0.750; coldpipe test.

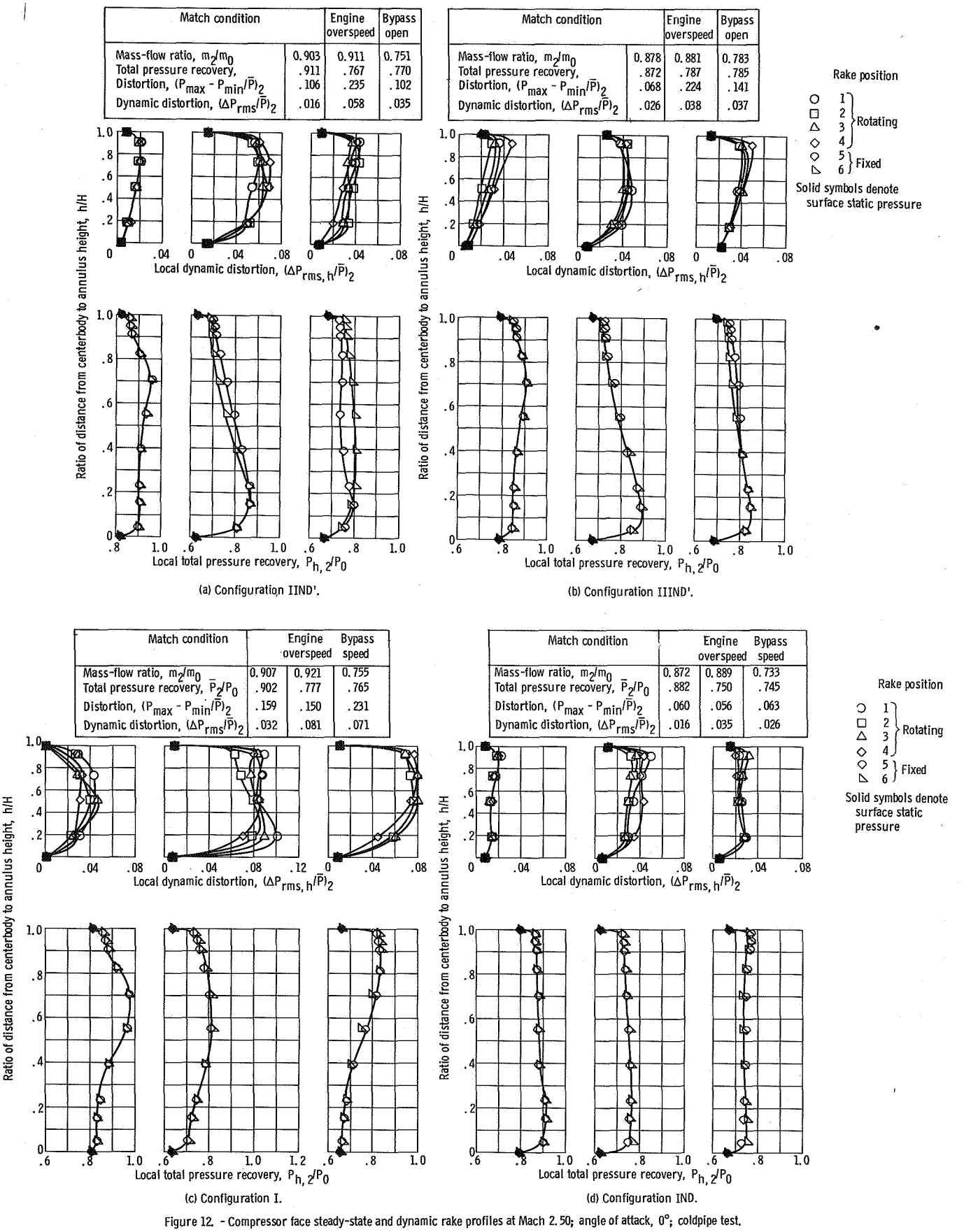

Figure 12. - Compressor face steady-state and dynamic rake profiles at Mach 2.50; angle of attack, 0°; coldpipe test.

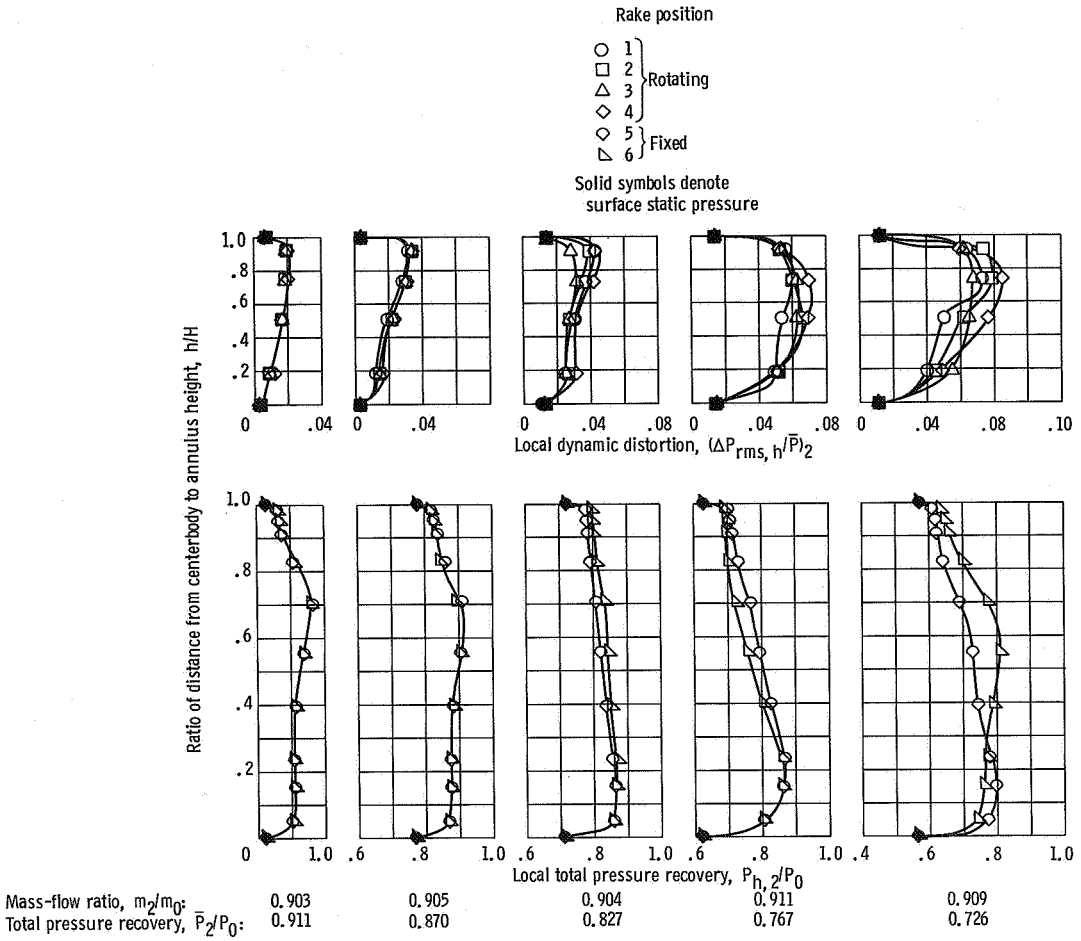

(a) Exit plug area variation.

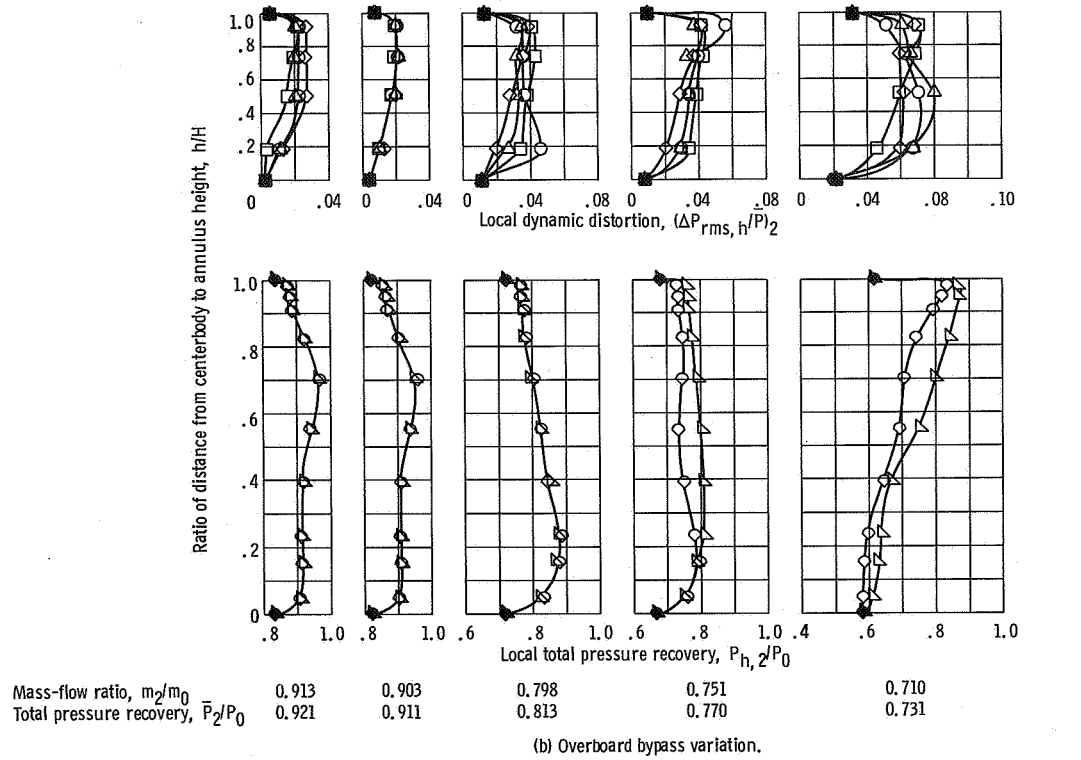

(b) Overboard bypass variation.

Figure 13. - Compressor face steady-state and dynamic rake profiles for configuration IIND; Mach 2.50; angle of attack, 0°; coldpipe test.

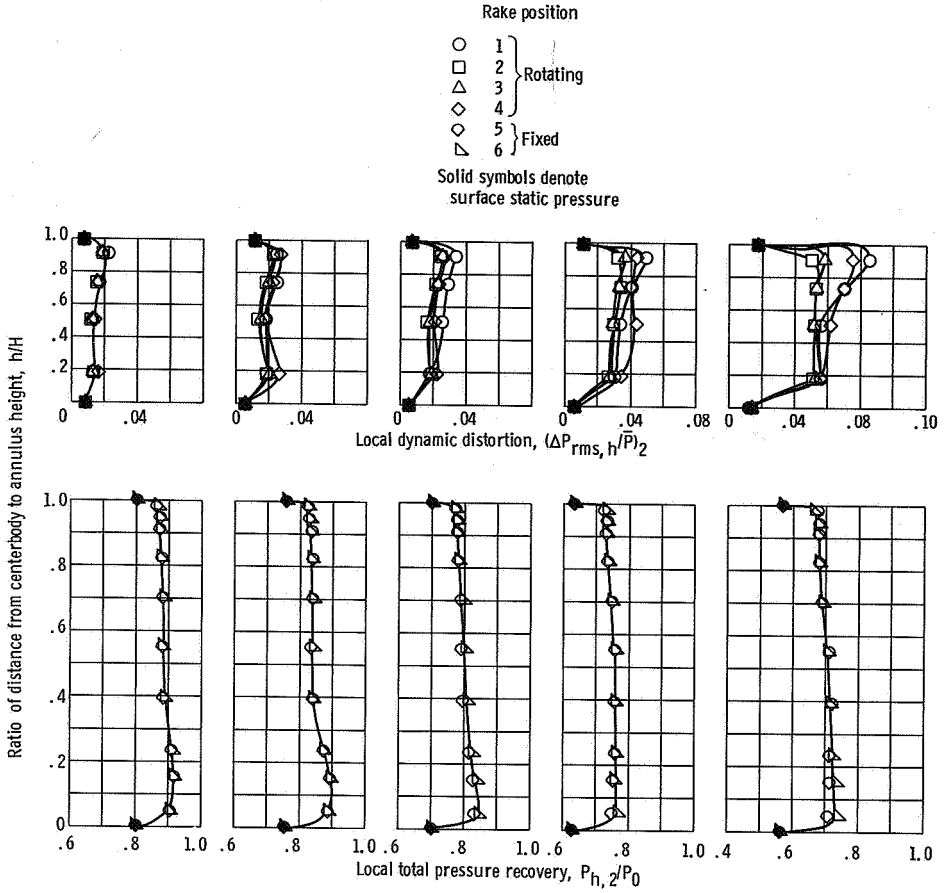

Mass-flow ratio, m_2/m_0	0.872	0.879	0.880	0.889	0.887
Total pressure recovery, $\bar{P}_2/P_0$	0.882	0.845	0.798	0.750	0.698

(a) Exit plug area variation.

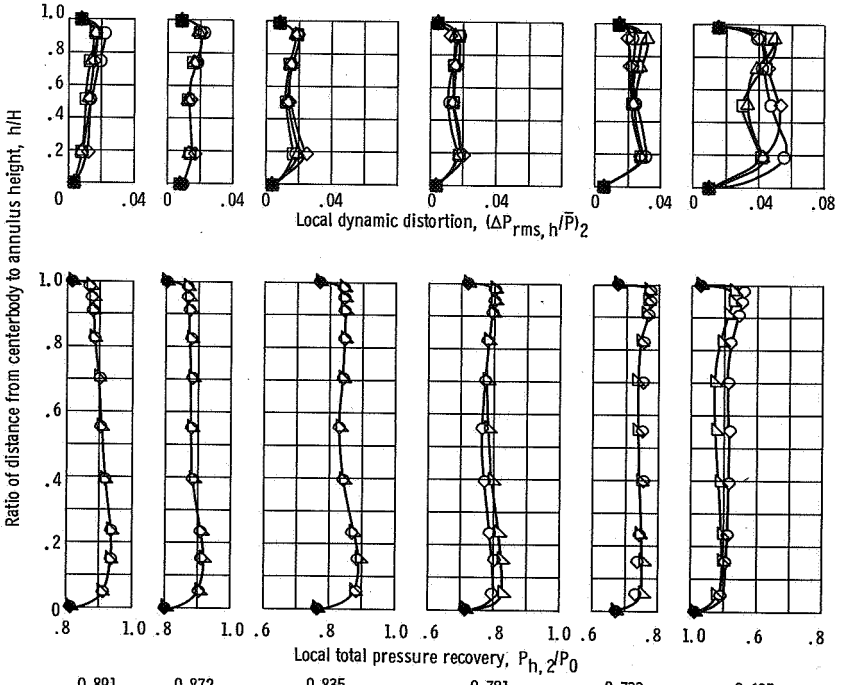

Mass-flow ratio, m_2/m_0	0.891	0.872	0.835	0.781	0.733	0.685
Total pressure recovery, $\bar{P}_2/P_0$	0.898	0.882	0.847	0.787	0.745	0.704

(b) Overboard bypass variation.

Figure 14. - Compressor face steady-state and dynamic rake profiles for configuration IND at Mach 2.50; angle of attack, 0; coldpipe test.

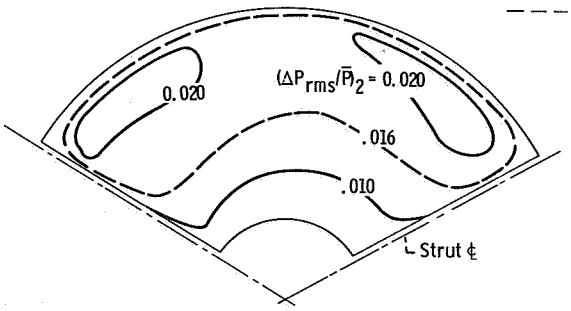

(a-1) Local dynamic distortion contours.

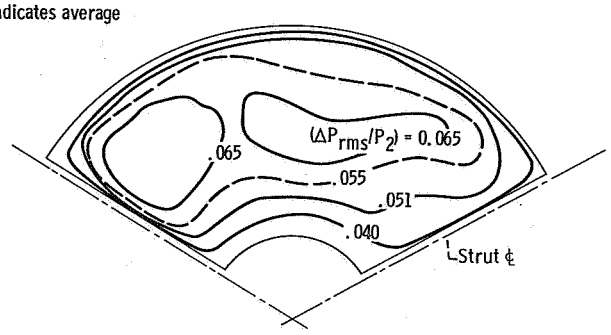

(b-1) Local dynamic distortion contours.

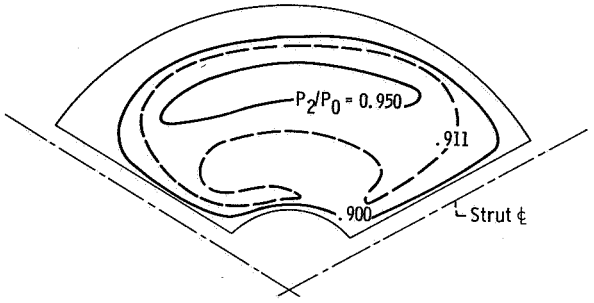

(a-2) Local pressure recovery contours.

(a) Mass-flow ratio, $m_2/m_0 = 0.903$; total pressure recovery, $\bar{P}_2/P_0 = 0.911$; cowl-lip-position parameter, $\theta_\ell = 26.5°$; free-stream Mach number, $M_0 = 2.50$.

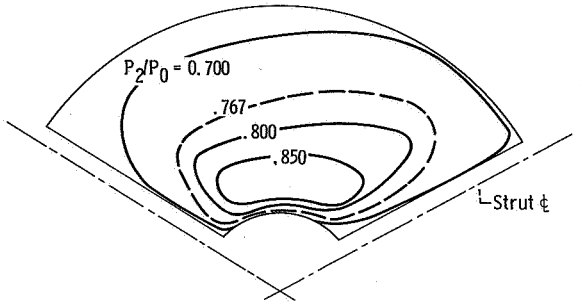

(b-2) Local pressure recovery contours.

(b) Mass-flow ratio, $m_2/m_0 = 0.911$; total pressure recovery $\bar{P}_2/P_0 = 0.767$; cowl-lip-position parameter, $\theta_\ell = 26.5°$; free-stream Mach number, $M_0 = 2.50$.

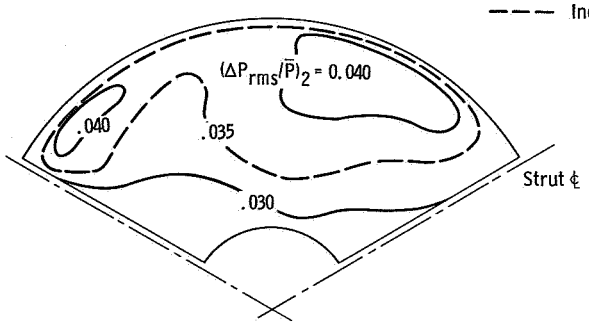

(c-1) Local dynamic distortion contours.

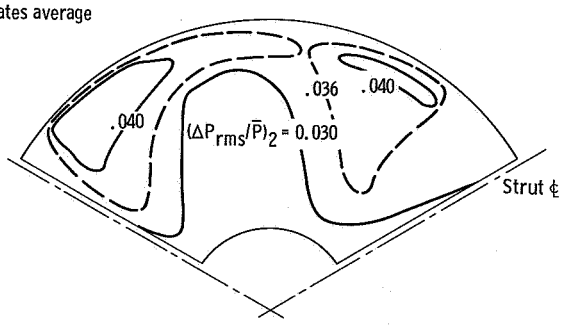

(d-1) Local dynamic distortion contours.

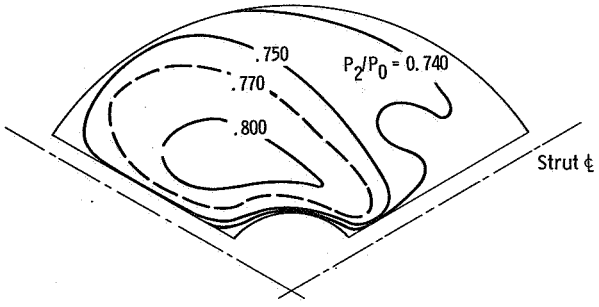

(c-2) Local pressure recovery contours.

(c) Mass-flow ratio, $m_2/m_0 = 0.751$; total pressure recovery, $P_2/P_0 = 0.770$; cowl-lip-position parameter, $\theta_\ell = 26.5°$; free-stream Mach number, $M_0 = 2.50$.

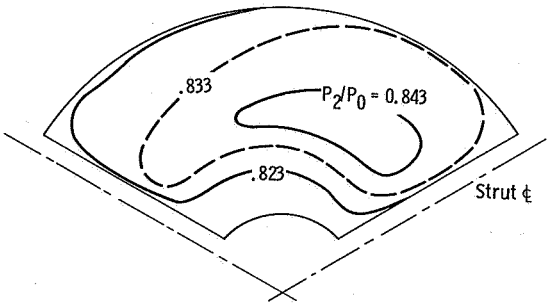

(d-2) Local pressure recovery contours.

(d) Mass-flow ratio, $m_2/m_0 = 0.829$; total pressure recovery $\bar{P}_2/P_0 = 0.833$; cowl-lip-position parameter, $\theta_\ell = 23.4°$; free-stream Mach number, 2.50; started inlet operation.

Figure 15. - Compressor face steady-state and dynamic total pressure contours for configuration IIND' at 0° angle of attack; coldpipe test.

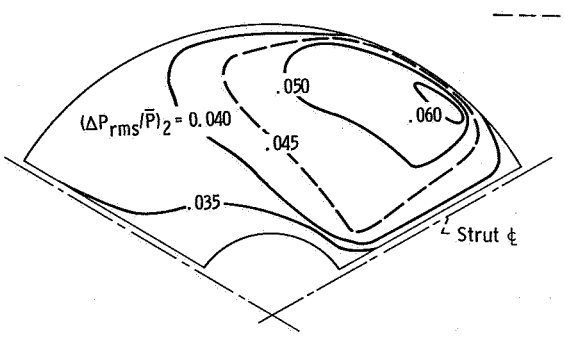

(e-1) Local dynamic distortion contours.

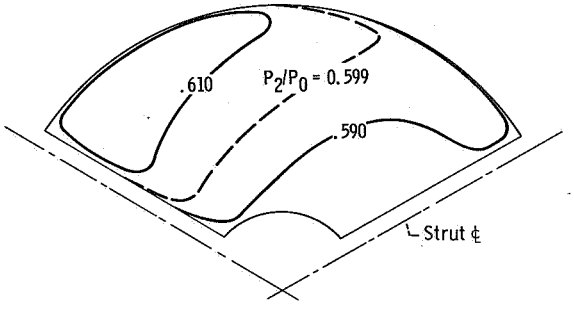

(e-2) Local pressure recovery contours.

(e) Mass-flow ratio, $m_2/m_0 = 0.613$; total pressure recovery, $\bar{P}_2/P_0 = 0.599$; cowl-lip-position parameter, $\theta_\ell = 23.4°$; free-stream Mach number, $M_0 = 2.50$; unstarted inlet operation.

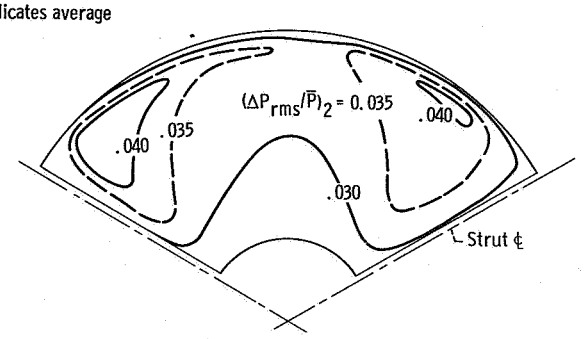

(f-1) Local dynamic distortion contours.

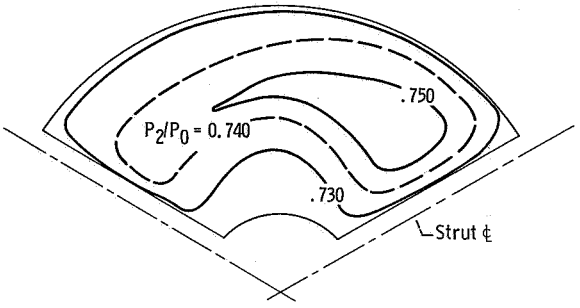

(f-2) Local pressure recovery contours.

(f) Mass-flow ratio, $m_2/m_0 = 0.733$; total pressure recovery, $\bar{P}_2/P_0 = 0.740$; cowl-lip-position parameter, $\theta_\ell = 20.9°$; free-stream Mach number, $M_0 = 2.50$; started inlet operation.

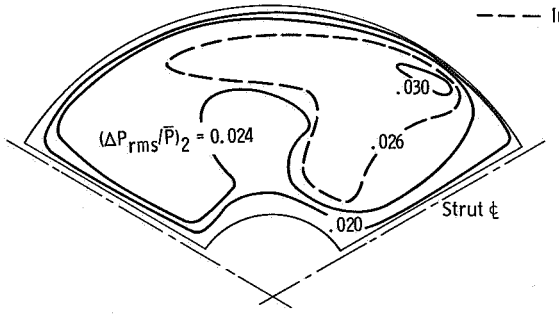

(g-1) Local dynamic distortion contours.

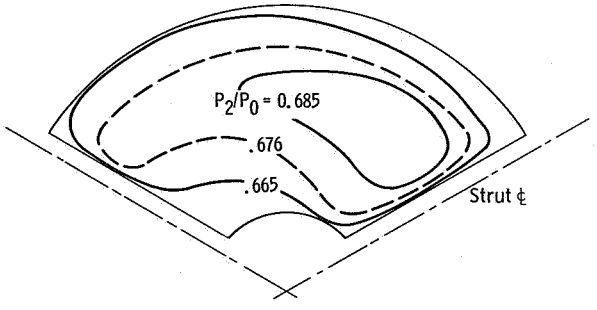

(g-2) Local pressure recovery contours.

(g) Mass-flow ratio, $m_2/m_0 = 0.673$; total pressure recovery, $\bar{P}_2/P_0 = 0.676$; cowl-lip-position parameter, $\theta_\ell = 21.2°$; free-stream Mach number, $M_0 = 2.50$; unstarted inlet operation.

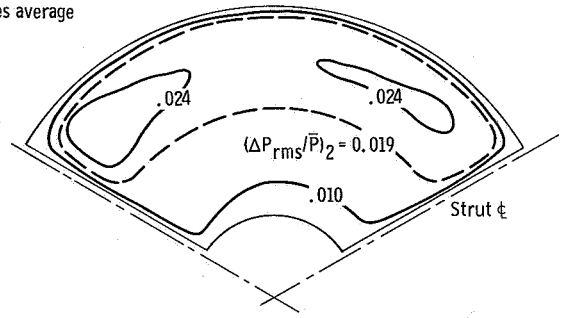

(h-1) Local dynamic distortion contours.

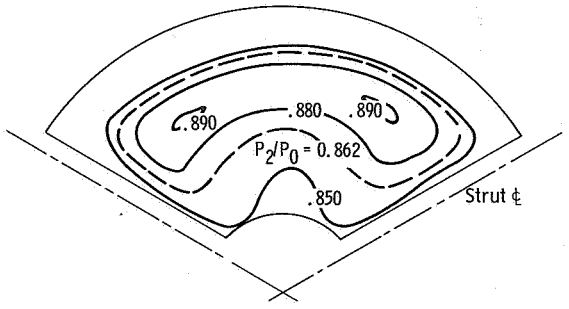

(h-2) Local pressure recovery contours.

(h) Mass-flow ratio, $m_2/m_0 = 0.921$; total pressure recovery, $\bar{P}_2/P_0 = 0.862$; cowl-lip-position parameter, $\theta_\ell = 26.0°$; free-stream Mach number, $M_0 = 2.58$.

Figure 15. - Continued.

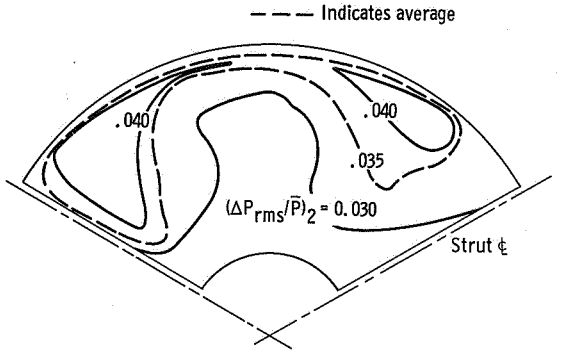

(i-2) Local dynamic distortion contours.

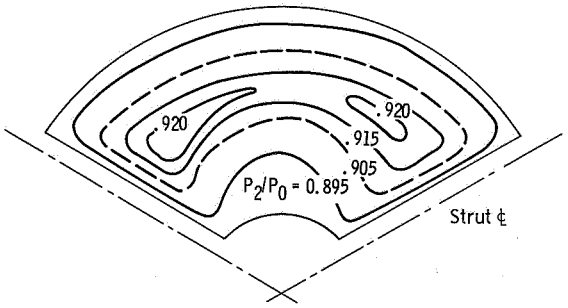

(i-2) Local pressure recovery contours.

(i) Mass-flow ratio, m_2/m_0 = 0.676; total pressure recovery, $\bar{P}_2/P_0$ = 0.905; cowl-lip-position parameter, θ_ℓ = 20.5°; free-stream Mach number, M_0 = 2.02.

Figure 15. - Concluded.

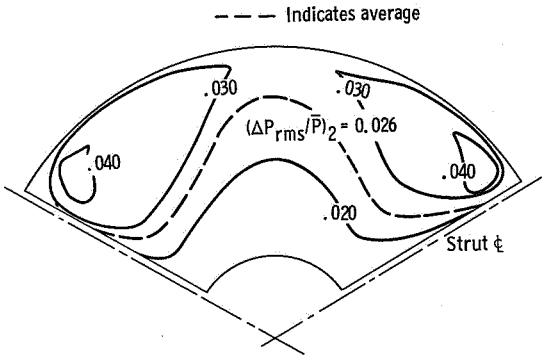

(a-1) Local dynamic distortion contours.

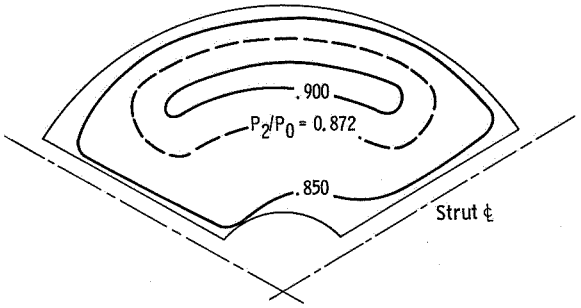

(a-2) Local pressure recovery contours.

(a) Mass-flow ratio, m_2/m_0 = 0.878; total pressure recovery, $\bar{P}_2/P_0$ = 0.872.

Figure 16. - Compressor face steady-state and dynamic total pressure contours for configuration III ND' at 0° angle of attack; cowl-lip-position parameter, θ_ℓ = 26.5°; free-stream Mach number, M_0 = 2.50; coldpipe test.

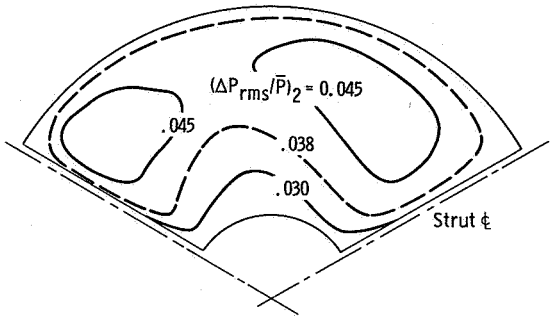

(b-1) Local dynamic distortion contours.

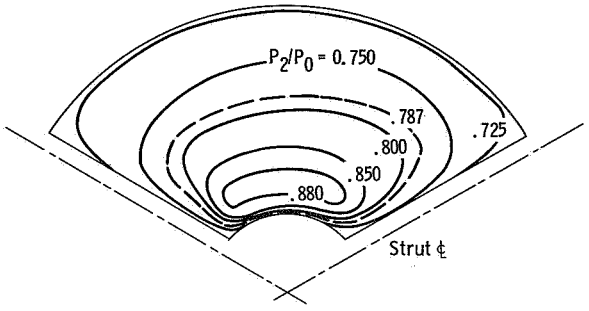

(b-2) Local pressure recovery contours.

(b) Mass-flow ratio, $m_2/m_0 = 0.881$; total pressure recovery, $\bar{P}_2/P_0 = 0.787$.

— — — Indicates average

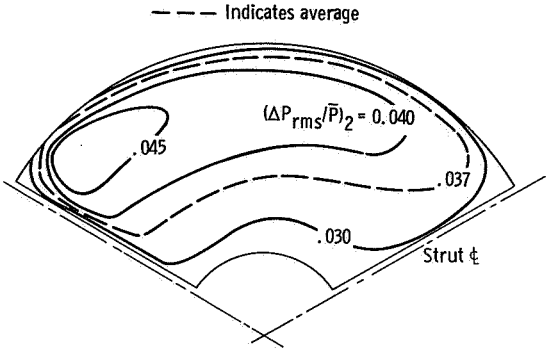

(c-1) Local dynamic distortion contours.

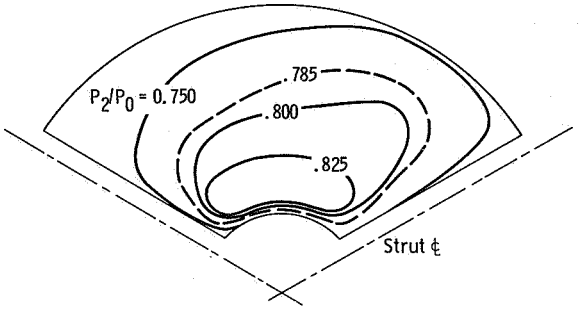

(c-2) Local pressure recovery contours.

(c) Mass-flow ratio, $m_2/m_0 = 0.783$; total pressure recovery, $P_2/P_0 = 0.785$.

Figure 16. - Concluded.

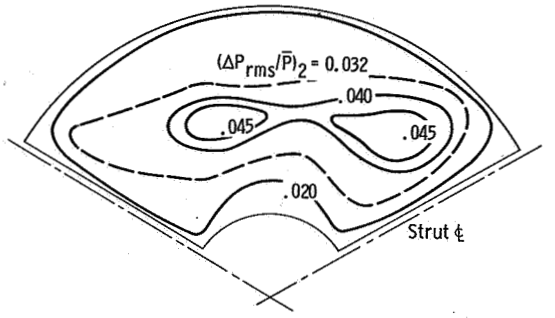

(a-1) Local dynamic distortion contours.

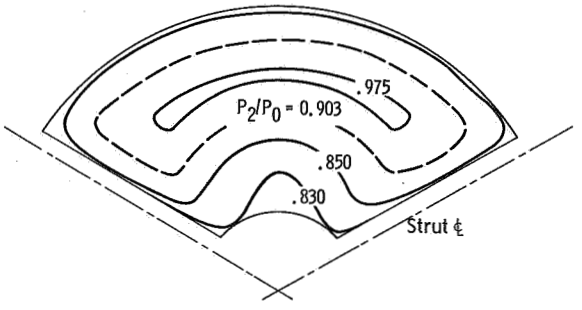

(a-2) Local pressure recovery contours.

(a) Mass-flow ratio, $m_2/m_0 = 0.907$; total pressure recovery, $\bar{P}_2/P_0 = 0.902$; cowl-lip-position parameter, $\theta_\ell = 26.5°$; free-stream Mach number, $M_0 = 2.50$.

— — — Indicates average

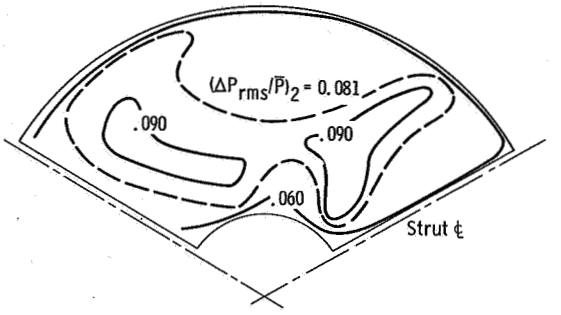

(b-1) Local dynamic distortion contours.

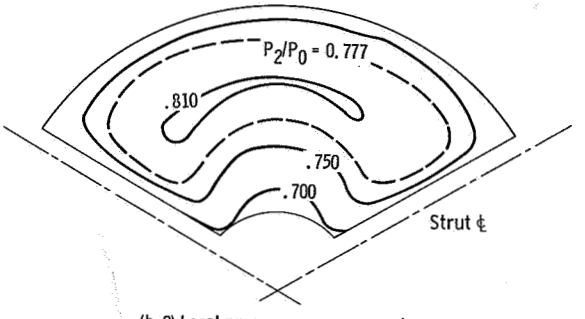

(b-2) Local pressure recovery contours.

(b) Mass-flow ratio $m_2/m_0 = 0.921$; total pressure recovery, $\bar{P}_2/P_0 = 0.777$; cowl-lip-position parameter, $\theta_\ell = 26.5°$; free-stream Mach number, 2.50.

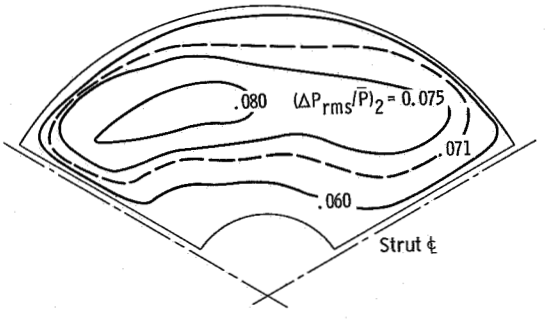

(c-1) Local dynamic distortion contours.

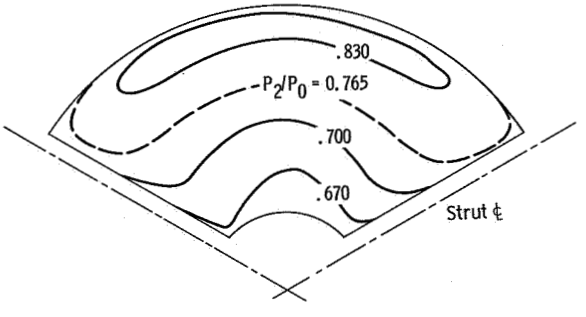

(c-2) Local pressure recovery contours.

(c) Mass-flow ratio, $m_2/m_0 = 0.755$; total pressure recovery $\bar{P}_2/P_0$ 0.765; cowl-lip-position parameter, $\theta_\ell = 26.5°$; free-stream Mach number, $M_0 = 2.50$.

— — — Indicates average

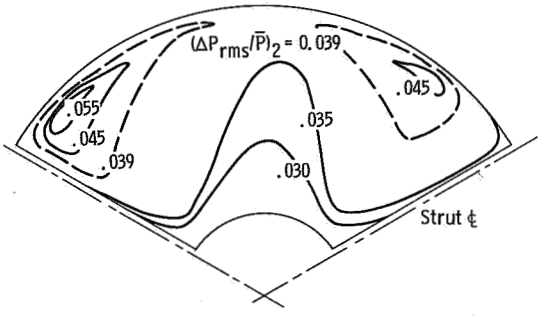

(d-1) Local dynamic distortion contours.

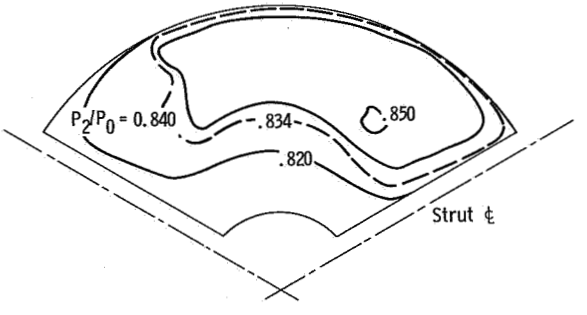

(d-2) Local pressure recovery contours.

(d) Mass-flow ratio, $m_2/m_0 = 0.827$; total pressure recovery, $\bar{P}_2/P_0 = 0.834$; cowl-lip-position parameter, $\theta_\ell = 23.4°$; free-stream Mach number, $M_0 = 2.50$.

Figure 17. - Compressor face steady-state and dynamic total pressure contours for configuration I at 0° angle of attack; coldpipe test.

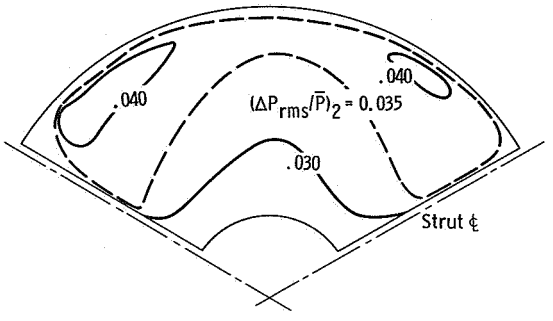

(e-1) Local dynamic distortion contours.

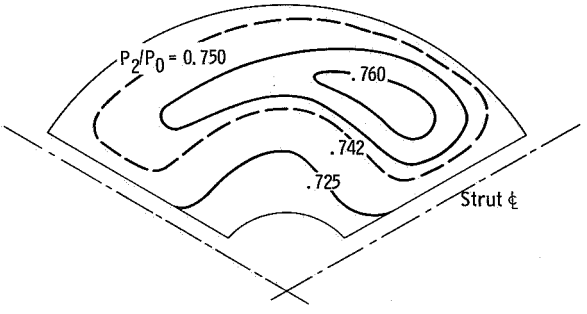

(e-2) Local pressure recovery contours.

(e) Mass-flow ratio, $m_2/m_0 = 0.735$; total pressure recovery, $\bar{P}_2/P_0 = 0.742$; cowl-lip-position parameter, $\theta_\ell = 20.9°$; free-stream Mach number, $M_0 = 2.50$; started inlet operation.

— — — Indicates average

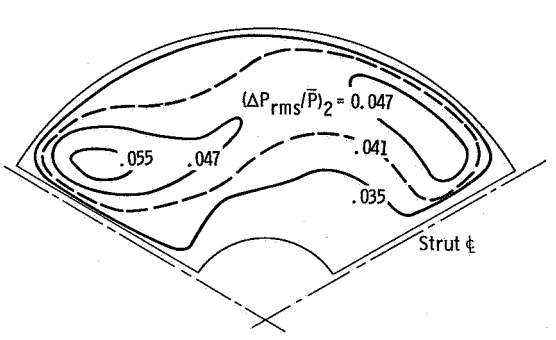

(f-1) Local dynamic distortion contours.

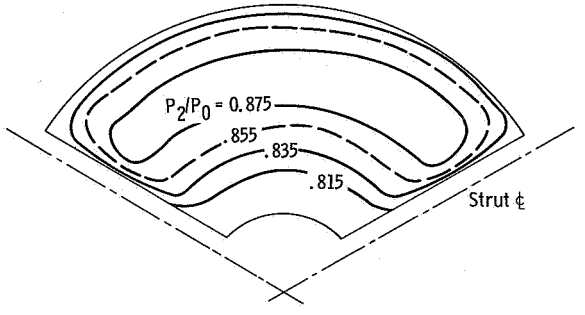

(f-2) Local pressure recovery contours.

(f) Mass-flow ratio, $m_2/m_0 = 0.926$; total pressure recovery, $\bar{P}_2/P_0 = 0.856$; cowl-lip-position parameter, $\theta_\ell = 26.0°$; free-stream Mach number, $M_0 = 2.58$.

Figure 17. - Concluded.

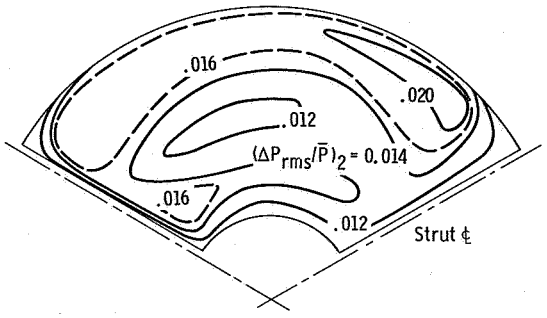

(a-1) Local dynamic distortion contours.

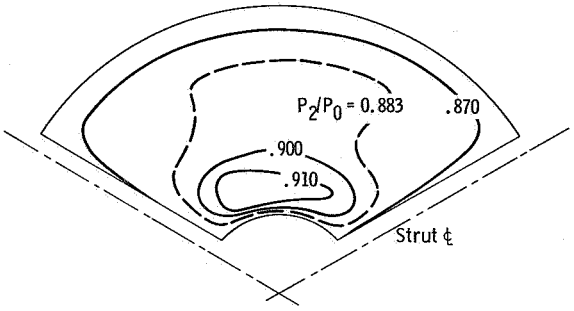

(a-2) Local pressure recovery contours.

(a) Mass-flow ratio, $m_2/m_0 = 0.872$; total pressure recovery, $\bar{P}_2/P_0 = 0.882$; cowl-lip-position parameter, $\theta_L = 26.5$; free-stream Mach number, $M_0 = 2.50$.

— — — Indicates average

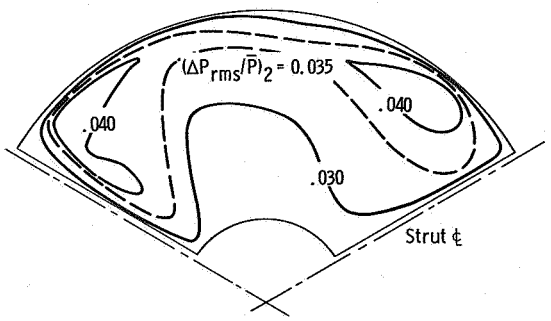

(b-1) Local dynamic distortion contours.

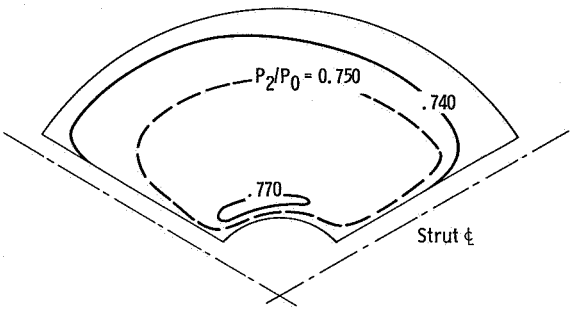

(b-2) Local pressure recovery contours.

(b) Mass-flow ratio, $m_2/m_0 = 0.889$; total pressure recovery, $\bar{P}_2/P_0 = 0.750$; cowl-lip-position parameter, $\theta_L = 26.5°$; free stream Mach number, $M_0 = 2.50$.

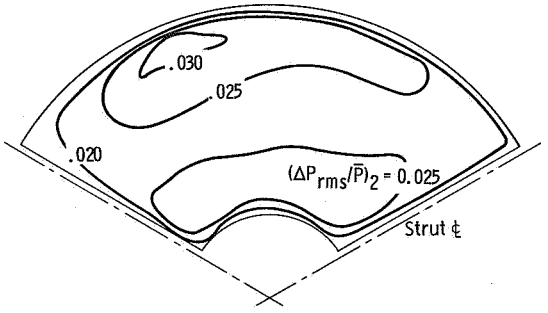

(c-1) Local dynamic distortion contours.

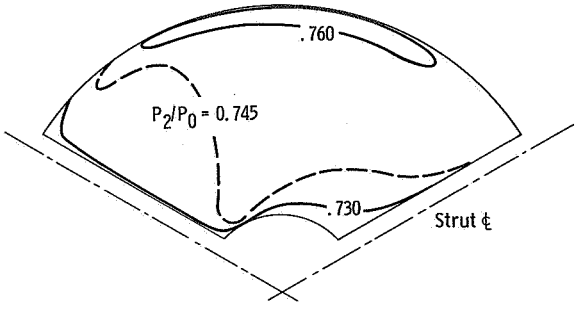

(c-2) Local pressure recovery contours.

(c) Mass-flow ratio, $m_2/m_0 = 0.755$; total pressure recovery, $\bar{P}_2/P_0 = 0.765$; cowl-lip-position parameter, $\theta_L = 26.5°$; free-stream Mach number, $M_0 = 2.50$.

— — — Indicates average

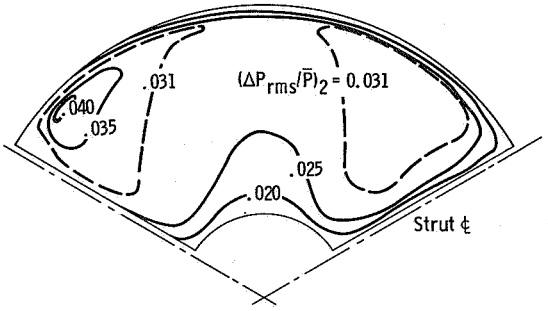

(d-1) Local dynamic distortion contours.

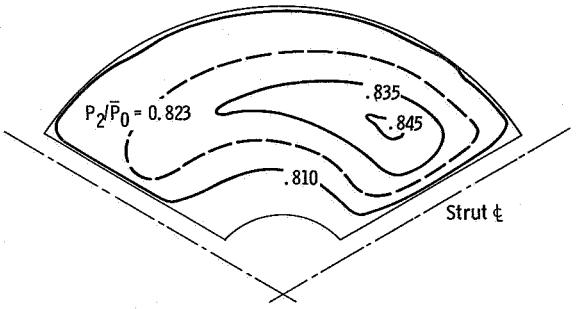

(d-2) Local pressure recovery contours.

(d) Mass-flow ratio, $m_2/m_0 = 0.816$; total pressure recovery, $\bar{P}_2/P_0 = 0.823$; cowl-lip-position parameter, $\theta_L = 23.4°$; free-stream Mach number, $M_0 = 2.50$; started inlet operation.

Figure 18. - Compressor face steady-state and dynamic total pressure contours for configuration IND at 0° angle of attack; coldpipe test.

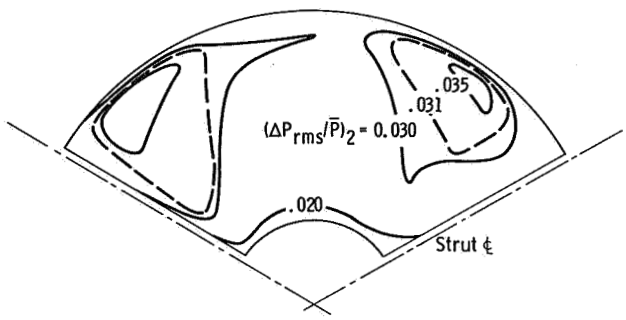

(e-1) Local dynamic distortion contours.

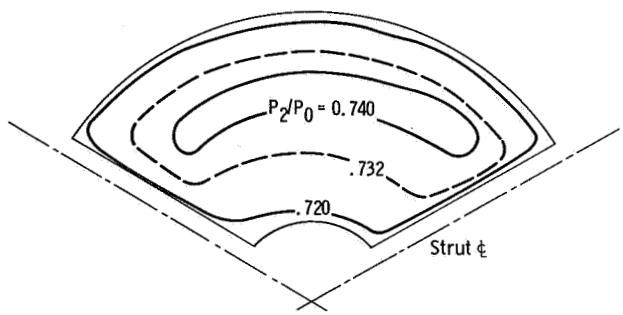

(e-2) Local pressure recovery contours.

(e) Mass-flow ratio, $m_2/m_0 = 0.723$; total pressure recovery, $\bar{P}_2/P_0 = 0.732$; cowl-lip-position parameter, $\theta_l = 20.9°$; free-stream Mach number, $M_0 = 2.50$.

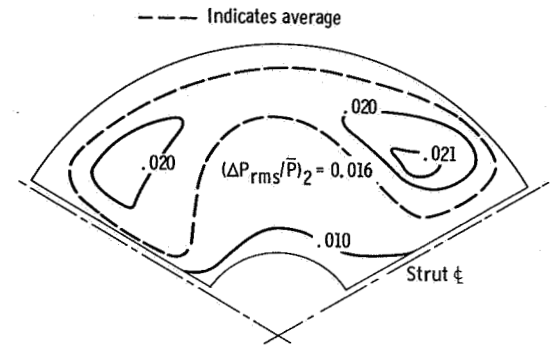

(f-1) Local dynamic distortion contours.

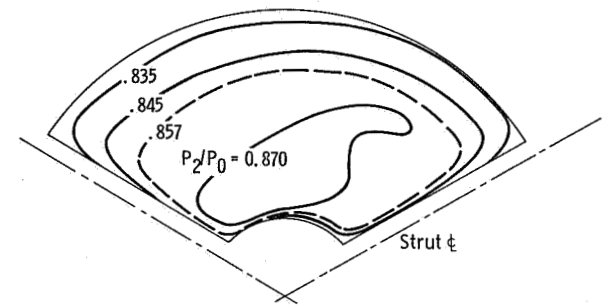

(f-2) Local pressure recovery contours.

(f) Mass-flow ratio, $m_2/m_0 = 0.923$; total pressure recovery, $\bar{P}_2/P_0 = 0.857$; cowl-lip-position parameter, $\theta_l = 26.0°$; free-stream Mach number, $M_0 = 2.58$.

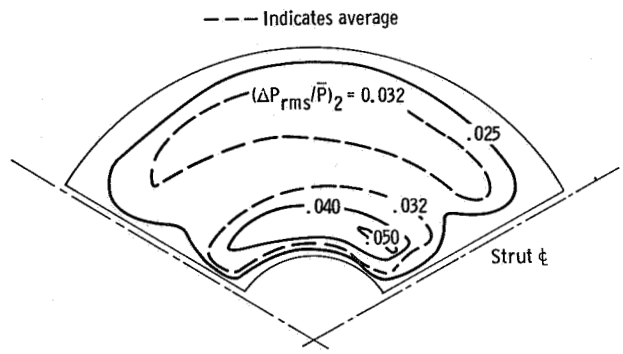

(g-1) Local dynamic distortion contours.

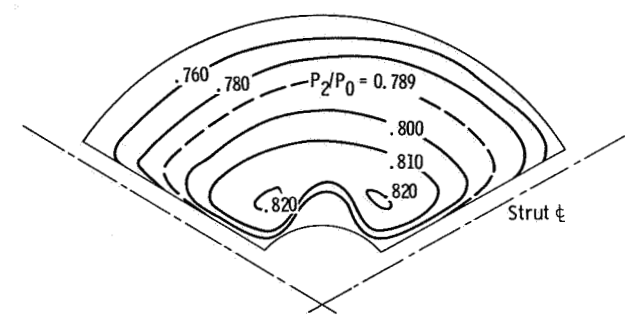

(g-2) Local pressure recovery contours.

(g) Mass-flow ratio, $m_2/m_0 = 0.936$; total pressure recovery, $P_2/P_0 = 0.789$; cowl-lip-position parameter, $\theta_l = 26.5°$; free-stream Mach number, $M_0 = 2.68$.

Figure 18. - Concluded.

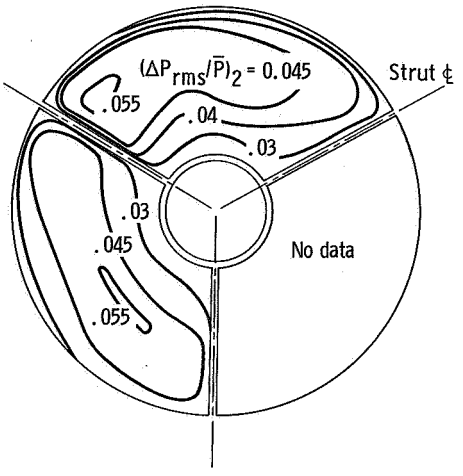

(a-1) Local dynamic distortion contours.

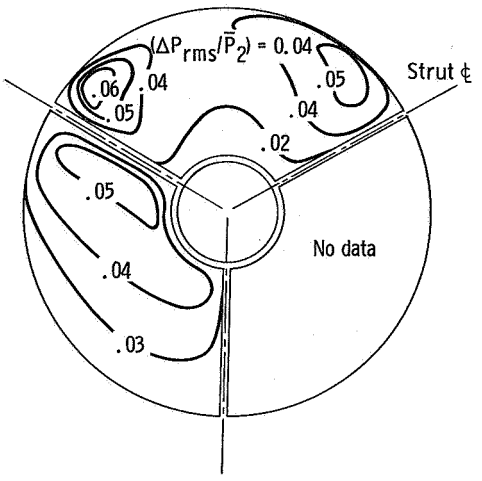

(b-1) Local dynamic distortion contours.

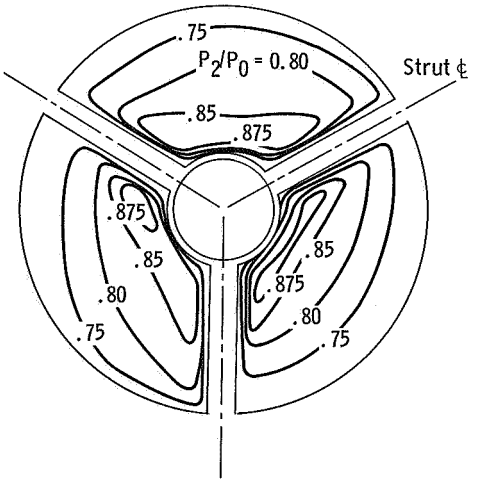

(a-2) Local pressure recovery contours.

(a) Angle of attack, $\alpha = 0°$; mass-flow ratio, $\frac{m_2}{m_0} = 0.842$; total pressure recovery, $\frac{\bar{P}_2}{P_0} = 0.793$.

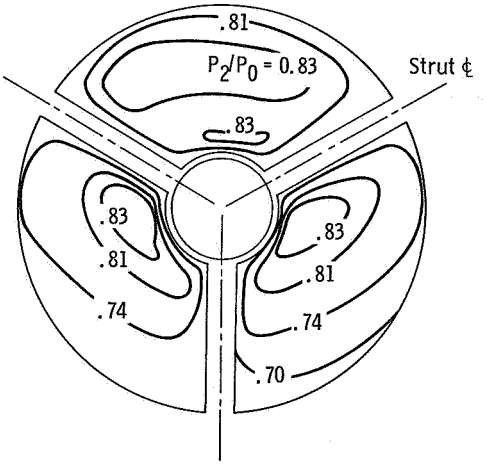

(b-2) Local pressure recovery contours.

(b) Angle of attack, $\alpha = 4.8°$; mass-flow ratio, $\frac{m_2}{m_0} = 0.844$; total pressure ratio, $\frac{\bar{P}_2}{P_0} = 0.792$.

Figure 19. - Compressor face steady-state and dynamic total pressure contours for configuration II ND' at Mach 2.58; coldpipe test.

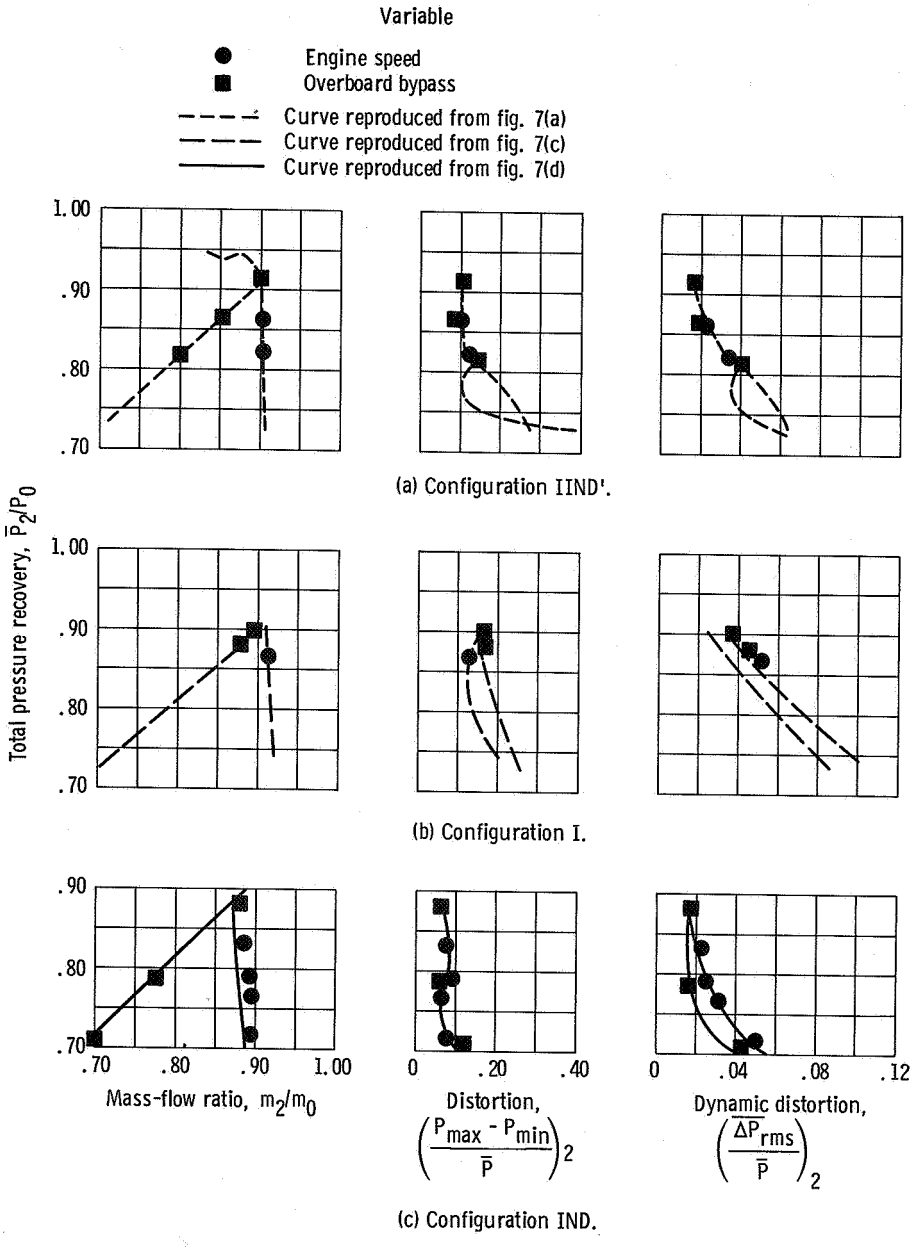

Figure 20. - Steady-state and dynamic inlet performance at Mach 2.50; angle of attack, 0°; engine test.

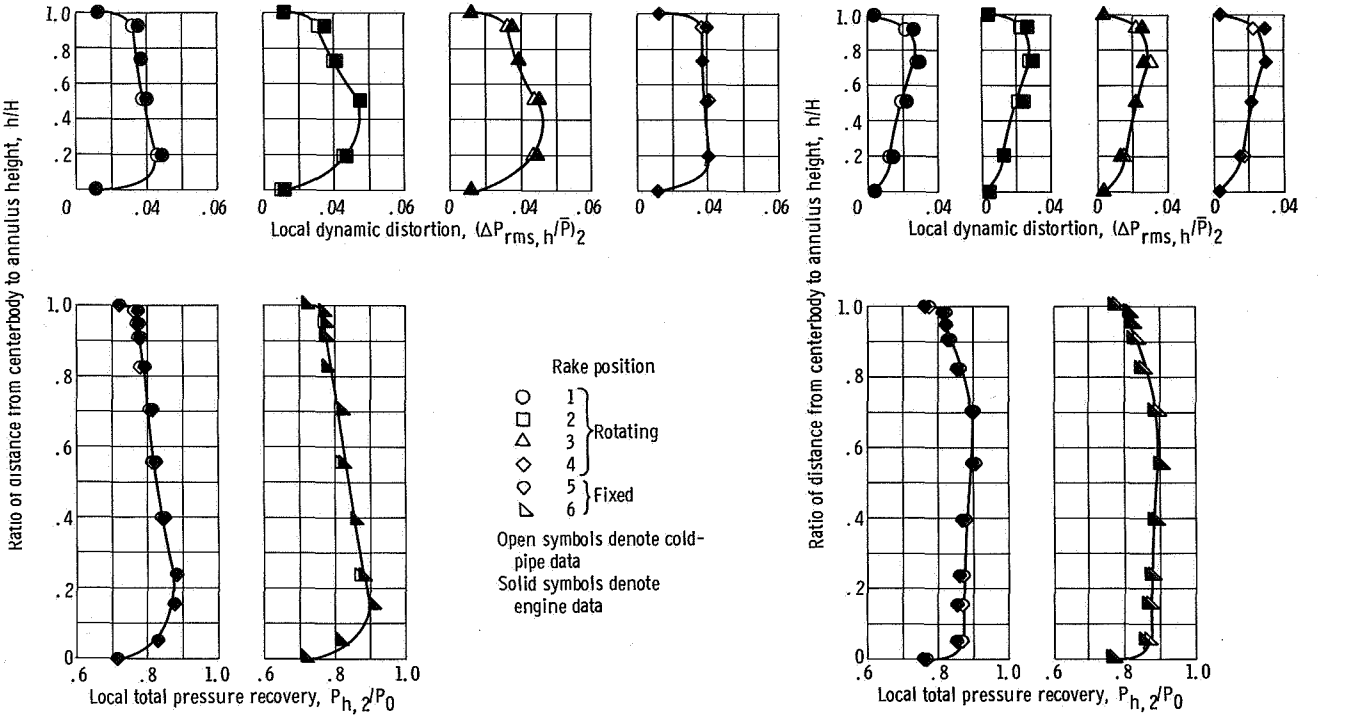

(a) Configuration IIND'; mass-flow ratio, $m_2/m_0 = 0.798$; total pressure recovery, $\bar{P}_2/P_0 = 0.813$; percent corrected engine speed, $(N/N^* \sqrt{\theta_2}) \times 100 = 86.6$.

(b) Configuration IIND'; mass-flow ratio, $m_2/m_0 = 0.905$; total pressure recovery, $\bar{P}_2/P_0 = 0.870$; percent corrected engine speed, $(N/N^* \sqrt{\theta_2}) \times 100 = 90.0$.

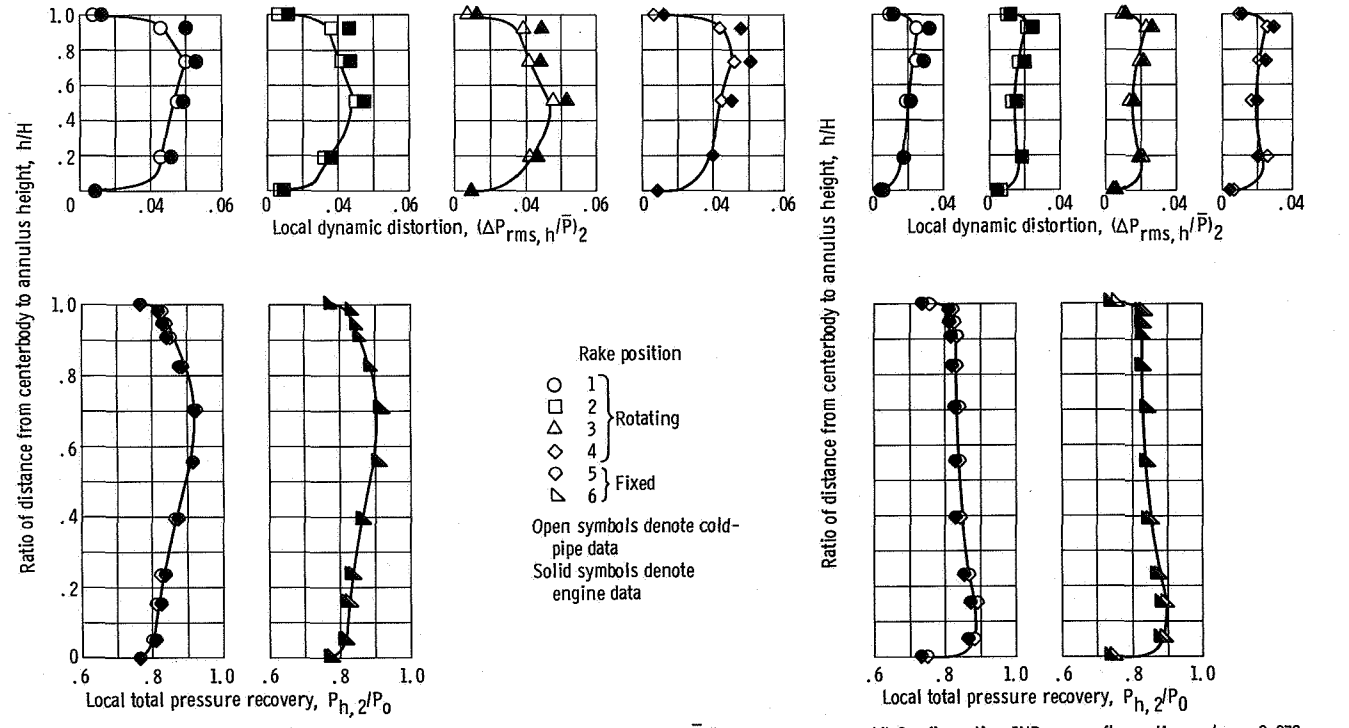

(c) Configuration I; mass-flow ratio, $m_2/m_0 = 0.916$; total pressure recovery, $\bar{P}_2/P_0 = 0.868$; percent corrected engine speed, $(N/N^* \sqrt{\theta_2}) \times 100 = 90.0$.

(d) Configuration IND; mass-flow ratio, $m_2/m_0 = 0.879$; total pressure recovery, $\bar{P}_2/P_0 = 0.845$; percent corrected engine speed, $(N/N^* \sqrt{\theta_2}) \times 100 = 90.0$.

Figure 21. - Effect of engine presence on compressor face steady-state and dynamic rake profiles at Mach 2.50 and 0° angle of attack.

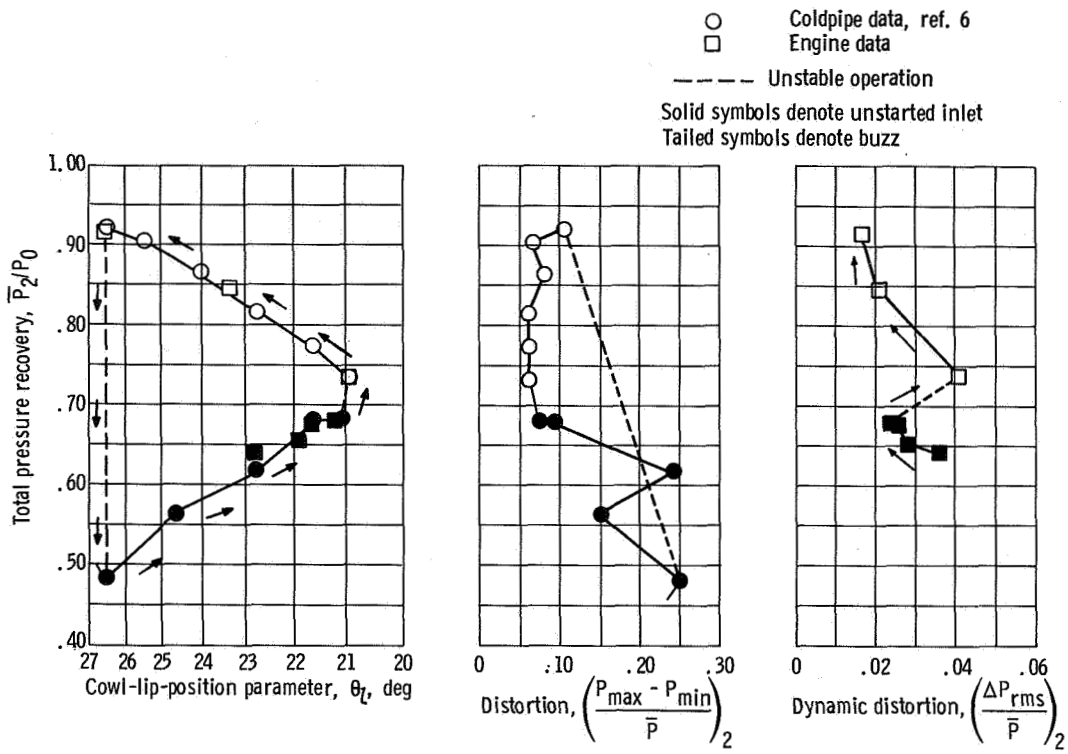

Figure 22. - Peak recovery restart cycle for configuration IIND' at Mach 2.50; angle of attack, 0°; match engine corrected weight flow.

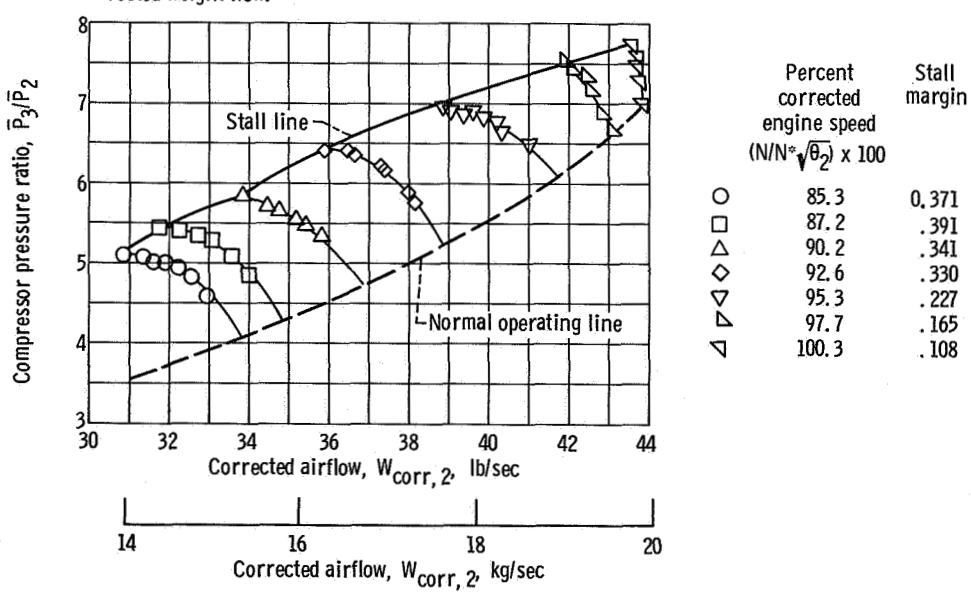

Figure 23. - Sea-level static stall line for undistorted inflow.

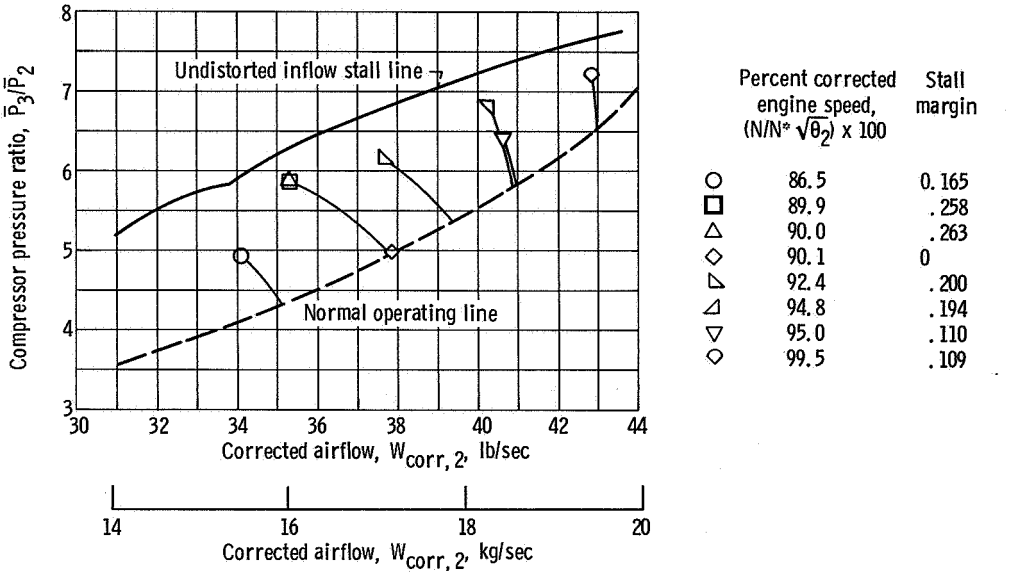

Figure 24. - Stall points obtained with configuration IND at Mach 2.50 and 0° angle of attack.

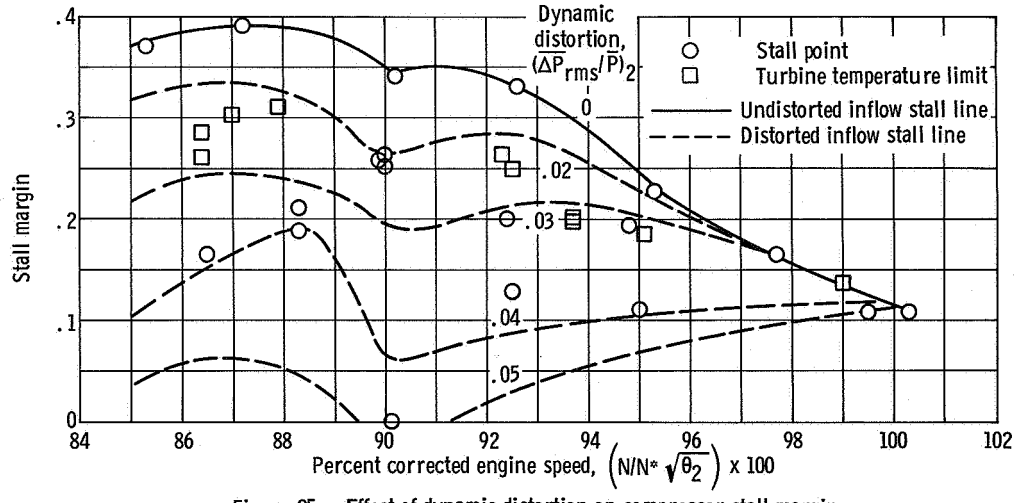

Figure 25. - Effect of dynamic distortion on compressor stall margin.

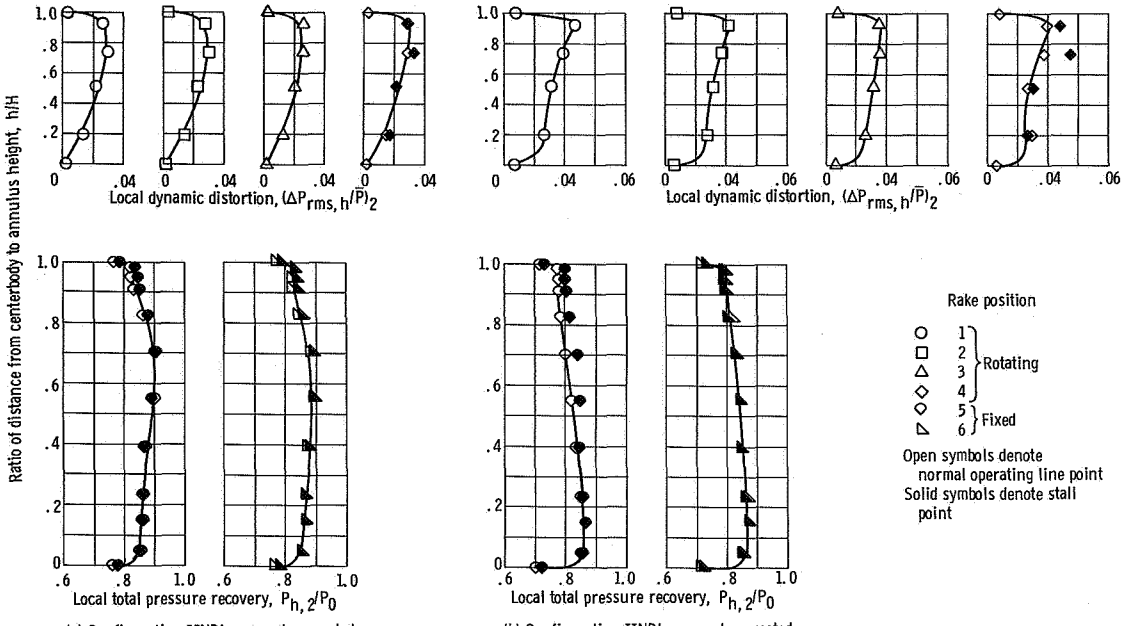

(a) Configuration IIND'; percent corrected engine speed, $(N/N^* \sqrt{\theta_2}) \times 100 = 90.0$; stall margin, 0.252.

(b) Configuration IIND'; percent corrected engine speed, $(N/N^* \sqrt{\theta_2}) \times 100 = 92.5$; stall margin, 0.129.

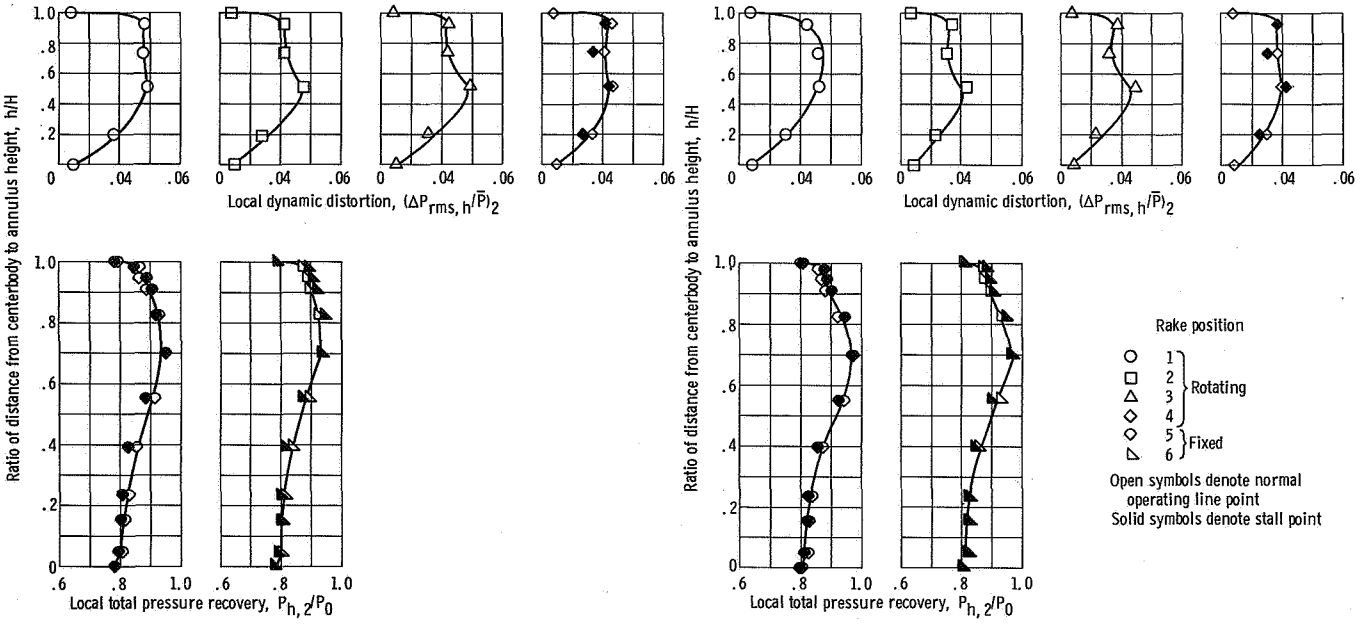

(c) Configuration I; percent corrected engine speed, $(N/N^* \sqrt{\theta_2}) \times 100 = 88.3$; stall margin, 0.211.

(d) Configuration I; percent corrected engine speed, $(N/N^* \sqrt{\theta_2}) \times 100 = 88.3$; stall margin, 0.189.

Figure 26. - Compressor face steady-state and dynamic rake profiles for inlet conditions prior to compressor stall at Mach 2.50 and 0° angle of attack.

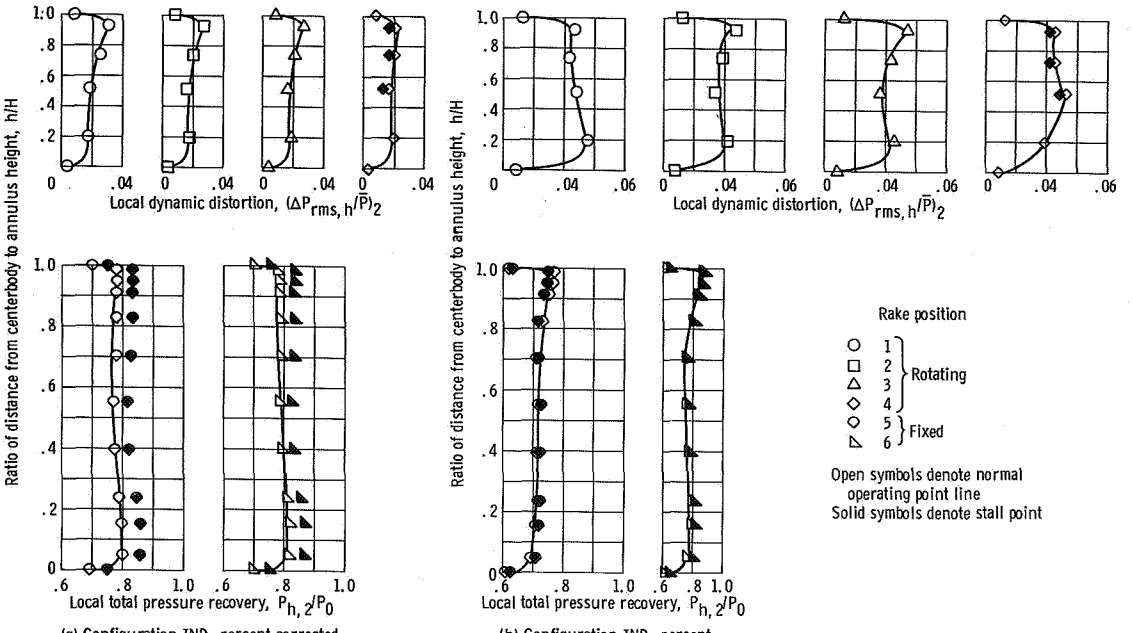

(g) Configuration IND; percent corrected engine speed, $(N/N^*\sqrt{\theta_2}) \times 100 = 90.0$; stall margin, 0.263.

(h) Configuration IND; percent corrected engine speed, $(N/N^*\sqrt{\theta_2}) \times 100 = 90.1$; stall margin, 0.

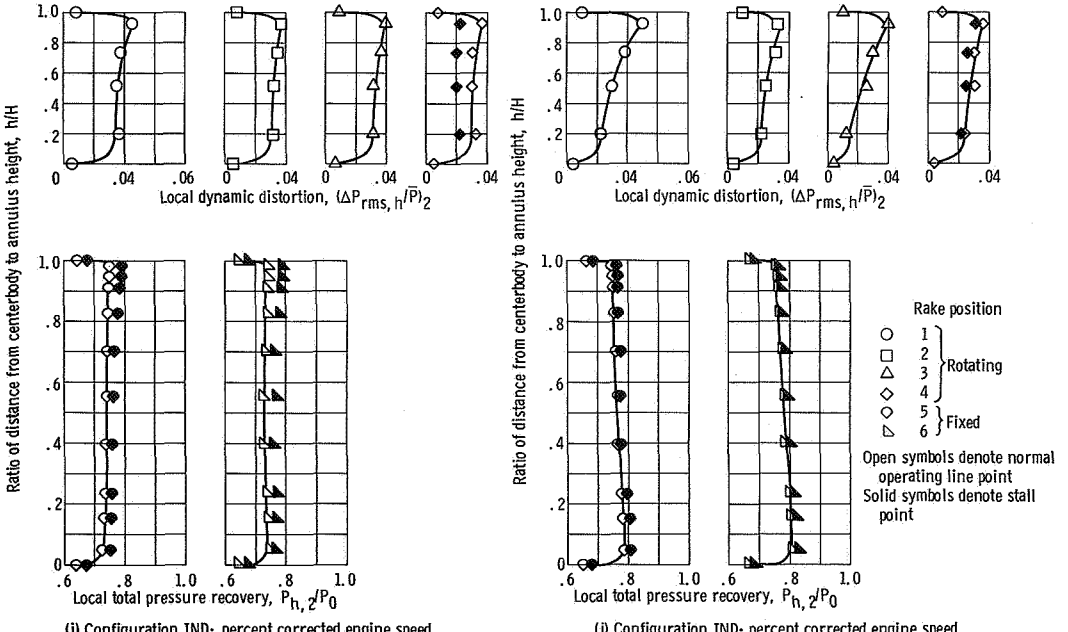

(i) Configuration IND; percent corrected engine speed, $(N/N^*\sqrt{\theta_2}) \times 100 = 92.4$; stall margin, 0.200.

(j) Configuration IND; percent corrected engine speed, $(N/N^*\sqrt{\theta_2}) \times 100 = 94.8$; stall margin, 0.194.

Figure 26. - Continued.

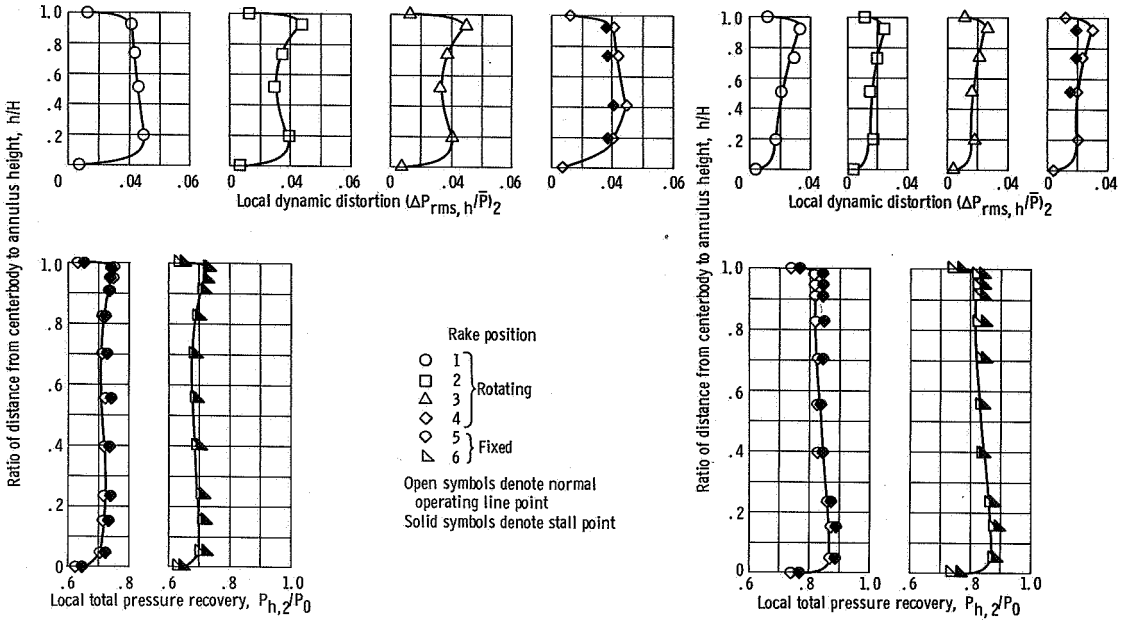

(e) Configuration IND; percent corrected engine speed, $(N/N^* \sqrt{\theta_2}) \times 100 = 86.5$; stall margin, 0.165.

(f) Configuration IND; percent corrected engine speed, $(N/N^* \sqrt{\theta_2}) \times 100 = 89.9$; stall margin, 0.258.

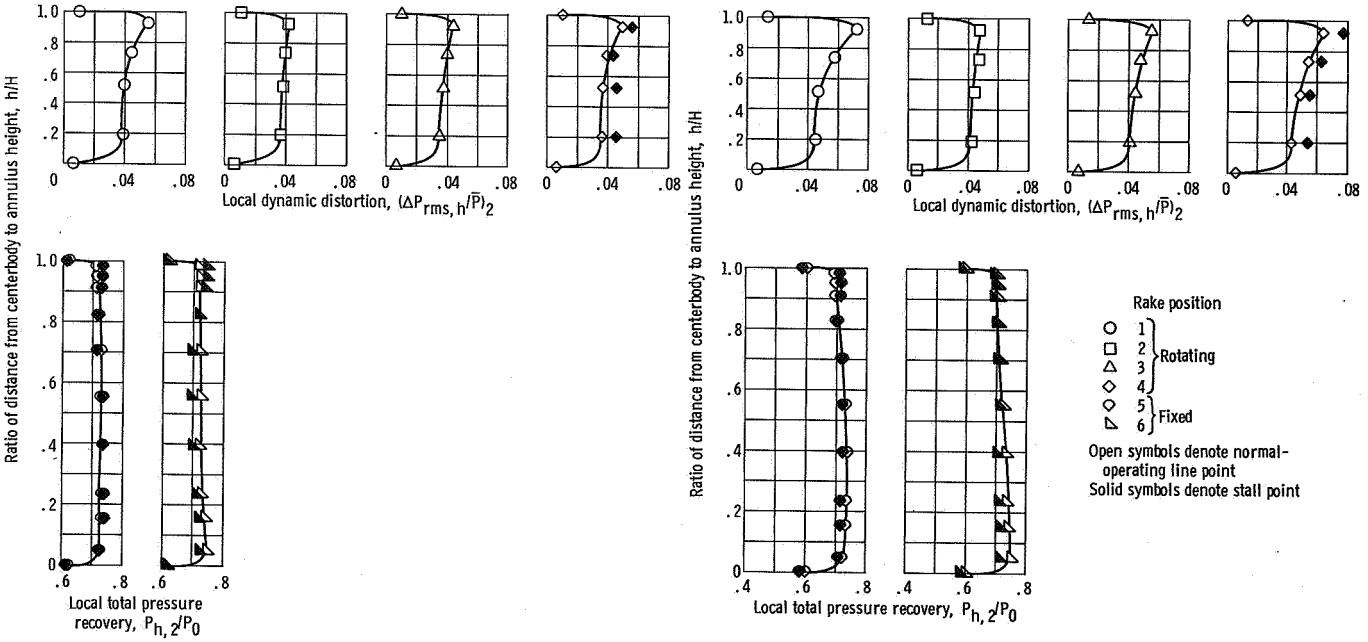

(k) Configuration IND; percent corrected engine speed, $(N/N^* \sqrt{\theta_2}) \times 100 = 95.0$; stall margin, 0.110.

(l) Configuration IND; percent corrected engine speed, $(N/N^* \sqrt{\theta_2}) \times 100 = 99.5$; stall margin, 0.109.

Figure 26. - Concluded.